

93 P.

NASA CR-54040
REPORT NO. 25,118



N64-26583

Code-1 Cat. 27
nasa cr-54040

MAGNETOGASDYNAMIC ROCKET FOR SPACE PROPULSION

BY

A.R. ASAM AND R.J. SUNDERLAND

PREPARED FOR

NATIONAL AERONAUTICS AND SPACE ADMINISTRATION
CONTRACT NAS 3-2514

OTS PRICE

XEROX

MICROFILM

\$

\$

8.60 ph.

THE MARQUARDT CORPORATION
MHD RESEARCH, INC.

NASA CR-54040
MR 25,118

SUMMARY REPORT

MAGNETOGASDYNAMIC ROCKET
FOR SPACE PROPULSION

by

Dr. R. J. Sunderland
Senior Staff Physicist
MHD Research, Inc.

A. R. Asam
Member of Advanced Technical Staff
The Marquardt Corporation

prepared for

NATIONAL AERONAUTICS AND SPACE ADMINISTRATION

20 May 1964

CONTRACT NAS 3-2514

Technical Management
NASA Lewis Research Center
Cleveland, Ohio
Space Electric Power Office

MHD Research, Inc.
P. O. Box 1815
Newport Beach, California

The Marquardt Corporation
16555 Saticoy Street
Van Nuys, California

TABLE OF CONTENTS

	<u>Page</u>
TABLE OF CONTENTS	i
LIST OF FIGURES	iii
 I. INTRODUCTION	 1
II. DESCRIPTION OF THE ACCELERATOR FACILITY	4
A. The Need For Vacuum Testing	4
B. The Engine	4
1. The Magnet	5
2. The Arc Electrodes	5
3. The Plasma Jet	10
4. Power Supplies	10
C. The Vacuum System	13
D. The Thrust Stand	16
1. General Considerations	16
2. Calibration of the Dynamometer	23
E. Instrumentation	25
1. Instrumentation Organization	25
2. Control Panel	27
3. Flow Meter	27
F. Engine Assembly	34
III. ENGINE PERFORMANCE	38
A. High Gas Flow Experiments	38
B. Low Gas Flow Experiments	43
1. Plasma Jet Performance	43
2. Argon-Helium Mixtures	43
3. Crossed Field Experiments	45
IV. DIAGNOSTICS	54
V. CONCLUSIONS	57
VI. REFERENCES	59
APPENDIX I - Accelerator Theory	60
A. List of Symbols	60
B. Fundamental Equations	62
C. Current Density Components	62
D. Velocity Interaction	63

TABLE OF CONTENTS cont'd

	<u>Page</u>
APPENDIX II - Thrust Measurement With Thin Flexure Dynamometry	64
APPENDIX III -	71
A. Heat Transfer and Friction Effects	71
B. Kinetic Theory Analysis	79
C. Hall Effects and Methods of Reducing Them	81
D. List of Symbols	82
E. References	85

LIST OF FIGURES

<u>Figure</u>		<u>Page</u>
1	Crossed Field Accelerator Geometry	2
2	The Magnet Assembly	6
3	Magnetic Flux Density As A Function Of Current	7
4	Electrode Assembly	8
5	Copper Anode	9
6	Photograph Of Arc Electrodes	11
7	Low Flow Anode Nozzle	12
8	Volt-Ampere Characteristics Of Arc Power Supply	14
9	The Test Chamber	15
10	Layout Of Vacuum System	17
11	The Vacuum Chamber	18
12	The Vacuum Chamber And Pumping System	19
13	Chamber Pressure As A Function Of Argon Throughput	20
14	The Dynamometer	22
15	Calibration System	24
16	Instrumentation Block Diagram	26
17	Control Panel Block Diagram	28
18	Controls And Instrumentation Console	29
19	Schematic Of Thermistor Flow Meter	30
20	Thermistor Resistance As A Function Of Temperature	32
21	Meter Current As A Function Of Water Flow	33
22	Partially Assembled Engine	35
23	Complete Engine Assembly	36
24	Crossed Field Region Of The Accelerator Anodes At Right	37
25	Accelerator Electrode Positions	39
26	Variation Of Plasma Jet Velocity As A Function Of Arc Current	44
27	Variation Of Arc Voltage As A Function Of Magnetic Field	46
28	Recorder Tracing Of Thrust Data	48
29a	Photograph Of Quartz Plate-Upper Plates	49
29b	Photograph Of Quartz Plate-Lower Plates	50
30	Electrode Arrangement (with electrodes parallel to flow direction)	52
31	Cardan Hinge	65
32	Regions Of Validity Of The Boundary Layer Analysis	75

FOREWORD

The experimental work on this contract was performed by Dr. R. J. Sunderland, Mr. C. Snyder and Mr. M. Minnamayer at MHD Research, Inc. under subcontract to The Marquardt Corporation. The analytical work on this contract was done by J. Baker, A. R. Asam and K. B. Cheney of The Marquardt Corporation.

MAGNETOGASDYNAMIC ROCKET

FOR SPACE PROPULSION

by

R. J. Sunderland and A. R. Asam

ABSTRACT

26583
A linear crossed field plasma accelerator and test facility was developed. Thrust measurements performed with the accelerator at gas flow rates of 0.1 grms/sec of argon were inaccurate and non-reproducible because of erosion of the accelerator electrode insulators. Severe material erosion limited continuous operation of the accelerator at magnetic fields above 500 gauss to a few minutes. Hall deflection was successfully reduced by staggering the accelerator electrodes.

Author:

MAGNETOGASDYNAMIC ROCKET

FOR SPACE PROPULSION

by

R. J. Sunderland, MHD Research, Inc.

and

A. R. Asam, The Marquardt Corporation

SUMMARY

A linear crossed field plasma accelerator and test facility was developed to investigate the feasibility of plasma propulsion for use in an extraterrestrial environment. The accelerator consisted of a plasma jet, supersonic nozzle and crossed electric and magnetic fields and was mounted on a dynamometer capable of measuring thrust in both the longitudinal and transverse directions. The entire unit was operated in a three foot diameter by six foot long vacuum chamber capable of maintaining a pressure of approximately 40 microns Hg with gas flow rates of 0.1 gms/sec of argon. There were 40 KW of power available for arc jet operation and 75 KW for accelerator operation. A description of the accelerator and test facility is provided along with some representative data for approximately 20 hours of intermittent operation.

It was determined that the accelerator could only be operated continuously for a period of a few minutes, at magnetic fields above 500 gauss, primarily because of severe material erosion. Hall deflection was effectively reduced by employment of staggered electrodes, however, arc erosion of the electrode insulators precluded accurate and reproducible thrust measurements. The principal difficulty occurred from the tendency of the arcs to migrate along the electrode leads when the external magnetic field was applied. The erosion of insulating plates on the top and bottom of the accelerator section was also severe.

I. INTRODUCTION

MHD Research, Inc. under subcontract to The Marquardt Corporation, has developed a linear crossed-field plasma accelerator and test facility to investigate the feasibility of plasma propulsion for use in an extraterrestrial environment. An associated analytical program was performed by The Marquardt Corporation.

The objectives of the experimental investigations were: (a) to improve the multiple discharge electrode arrangement, previously developed under Contract NAS-5-1120, with respect to stability of arc discharges, suppression of Hall effects, and the minimization of channel friction, heat transfer, and electrode erosion; (b) to investigate more efficient methods of diagnostic experiments to determine the electron density and temperature as a function of position of the plasma in the accelerator; and (d) to develop a reliable measuring system to obtain reproducible data on thrust level, specific impulse, particle velocity, and mass flow, with and without application of electromagnetic accelerating forces.

The objectives of the analytical investigation were: (a) to determine the heat transfer and frictional effects applicable to the desired range of mass flow and specific impulse in the presence of crossed electric and magnetic fields; (b) to determine optimum channel geometries; (c) to study the Hall phenomena and methods of reducing Hall effects; and (d) to perform an overall propulsion analysis which would lead to the selection of performance parameters securing optimum performance.

Before definitive results were obtained, the analytical portion was deleted from the program at the request of the Lewis Research Center in order to supply a larger effort to the experimental investigation.

In the experiments to be described, a partially ionized gas having cylindrical symmetry about the Z axis is initially moving parallel to this axis, Figure 1. The gas enters a region in which the magnetic induction, B , is parallel to the negative X axis and which has an electric field in the XY plane having both Y and Z components. Actually, the gas enters and leaves the crossed field region through a fringing magnetic field so that the magnetic induction at the inlet and exit regions has components in the Z as well as in the X directions. The jet is bounded in the X direction by the insulated pole faces of an electromagnet, but is unbounded in the Y direction except for the electrodes which establish the electric fields. The YZ plane of the accelerator was horizontal and the XZ plane vertical in the gravitational sense.

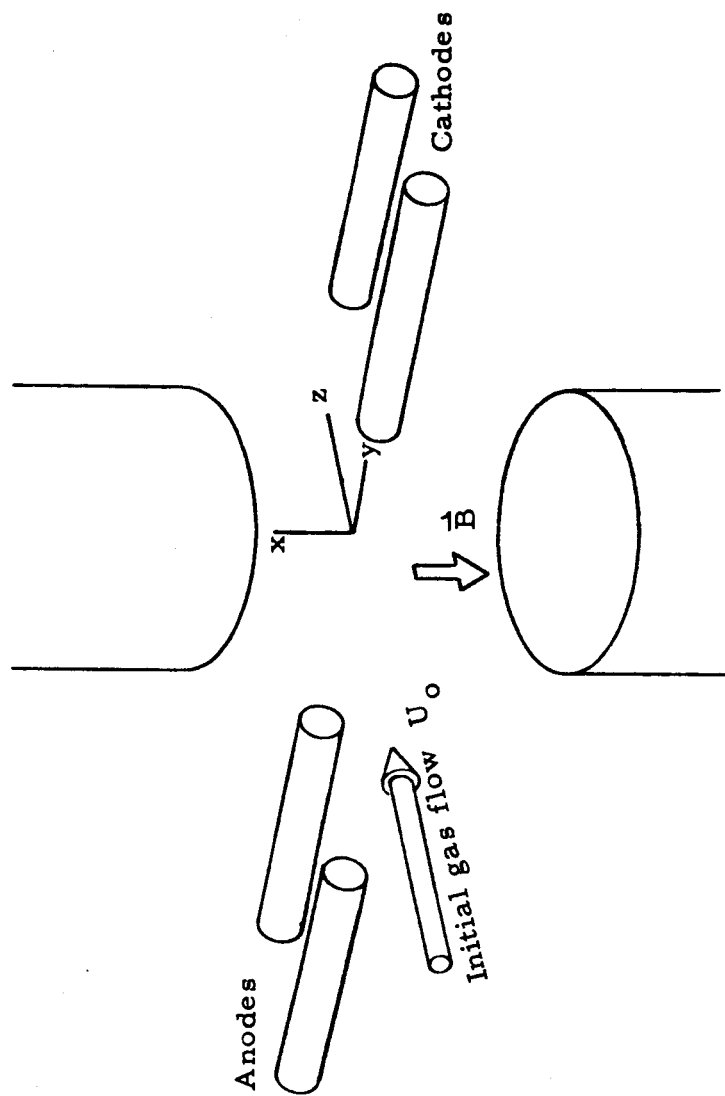


Figure 1. Crossed field accelerator geometry.

The thrust increment imparted to the partially ionized gas stream by the accelerator may, in principle, be ascertained by integrating the $\vec{J} \times \vec{B}$ term in the equation of motion over the interaction volume.

However, the current density term \vec{J} is a function of the components of the magnetic induction \vec{B} , the scalar electrical conductivity σ_0 in the zero magnetic field case, and the Hall and ion-slip parameters σ_1 and σ_2 (as defined in Appendix I), as well as a function of the electric field E as measured in a frame of reference moving with the velocity u of the plasma as a whole. In general, the problem involves the solution of the fundamental magnetohydrodynamic equations for the variables ρ , p , T , \vec{u} , \vec{j} , \vec{E} and \vec{B} . These equations are shown in Appendix I along with the definitions of the appropriate symbols.

Several authors (e.g., Ref 1-7) have attempted to obtain solutions for this set of equations. However, the assumptions which must be made in order to yield mathematically tractable forms (e.g., constant density, uniform temperatures, constant degree of ionization, uniform magnetic induction, well defined boundaries, etc.) removes the results from the region of those actually observed. Therefore, rather than attempt to improve upon existing theoretical treatments it was decided to adopt an engineering approach to the problem.

The accelerator and plasma jet were mounted on a thrust stand capable of yielding both the longitudinal and transverse thrust components. By recording the thrust observed for various applied magnetic fields, arc voltages and currents, electrode geometries, gas flow rates and plasma jet powers, correlations could be made which would yield thrust data as a function of the engine operating parameters. These correlations would be appropriate to this one engine only, and would not be representative of crossed-field accelerators in general. The degree of success of this approach will be discussed in the sections below.

II. DESCRIPTION OF THE ACCELERATOR FACILITY

A. THE NEED FOR VACUUM TESTING

Previous crossed-field accelerator experiments performed in the MHD Research, Inc. laboratories were conducted in an environment which did not represent true space-like conditions and which were not conducive to obtaining accurate thrust measurements. In these tests, the plasma generator was located outside the vacuum system, while the magnet pole faces and arc electrodes were mounted inside a vacuum container. The pressure in the system was several millimeters of mercury and thrust measurements were made by allowing the plasma beam to impinge upon a thrust disk. Calibration of the thrust disk was based on the assumptions that the plasma beam fell upon the center of the thrust disk and was deflected through an angle of 90° , and that no material was ejected from the face of the disk itself. In addition, it was assumed that effects due to thermal distortions were negligible. In reality, the beam did not strike the center of the disk, but was deflected towards the edges due to the interaction between the magnetic field and axial currents in the plasma. No experiments were conducted to determine the effects of ablation from the face of the disk. Consequently, thrust measurements are considered to have inaccuracies from 0 to 20 percent.

To alleviate these objections the plasma accelerator in the present program is operated as an engine in a more realistic space environment. The plasma generator, magnet, and crossed-field arcs are located in a vacuum chamber maintained at a pressure of several microns of Hg, and thrust measurements are made by observing the deflections of the entire engine unit. The arc region is maintained at a pressure of from 200 micron to several millimeters, and the beam passes through an exit nozzle into the region of lower vacuum. In the sections below, descriptions are given of the engine, the vacuum system, the thrust stand, and the instrumentation used to monitor engine and thrust stand operation.

B. THE ENGINE

The $\vec{J} \times \vec{B}$ engine assembly consists of a plasma generator to provide a flow of partially ionized gas, a supersonic nozzle to partially convert the thermal energy of the plasma to directed kinetic energy, a set of arc electrodes, and an electromagnet. The directions of the magnetic field, the electric field and the initial velocity vector of the gas flow are mutually perpendicular.

1. The Magnet

The magnet assembly, as shown in Figure 2, has an H configuration and is utilized as the engine frame. The E field electrodes are mounted in iron holders which fit into the magnet yoke. The plasma generator and supersonic nozzle are also mounted to the magnet yoke. The interior working area of the magnet is enclosed in water-cooled shrouding with a wide open region on the downstream side. This shrouding is necessary to provide a higher pressure in the arc region than exists in the vacuum tank itself. The pressure in the environmental chamber is in the range of 10 - 1000 microns of mercury, depending upon gas flow rates.

The electromagnet is designed for 90,000 ampere turns and has a 3 inch gap. The pole cores have a diameter of 6 inches and the removable water-cooled pole shoes are 6 inches in diameter chamfered to a working area of approximately 4 inches by 6 inches. The coils, three on each pole core, are 15-1/8" outside diameter. The multiple coils provide for more versatility in electrical hookup and also provide for more efficient cooling. A water-cooled copper heat sink is placed between each coil and in all there are eight heat sinks. The magnet yoke is 19 inches by 19 inches by 8 inches, and is fabricated of low carbon steel. The windings on the coils are No. 14 gauge square copper wire with Polythermalex insulation. The entire structure is epoxied to form a compact, gas tight assembly. The resistance of each coil is less than 10 ohms at 300°K.

Figure 3 shows the magnetic flux density at the center of the field region as a function of the magnet current. These tests were performed without water cooling in the magnet coils and no excessive heating was observed at the highest current ratings. The curve shows no signs of saturation up to magnet currents of 6 amperes per coil. In the experiments to be described the magnetic field strength was always below 8000 gauss.

2. The Arc Electrodes

The E field electrodes, shown in Figure 4, are mounted in three pairs, 1-1/2 inches on centers. They are constructed of 3/4 inch diameter 2 percent thoriated tungsten which is water-cooled by coaxial squirt tube. The electrode shanks are encased in a refractory ceramic insulator (boron nitride). A special plumbing cross is mounted on the termination of each electrode to provide access for cooling water and electrical connections. In an attempt to force arc attachment to the electrodes in a magnetic field-free region the electrodes can be sheathed with a cylinder of soft iron. Anodes having the same design, but with copper tips as shown in Figure 5 have also been operated. The anodes were designed in this manner so that arc attachment would be confined to the elongated copper portion when the magnetic field was applied.

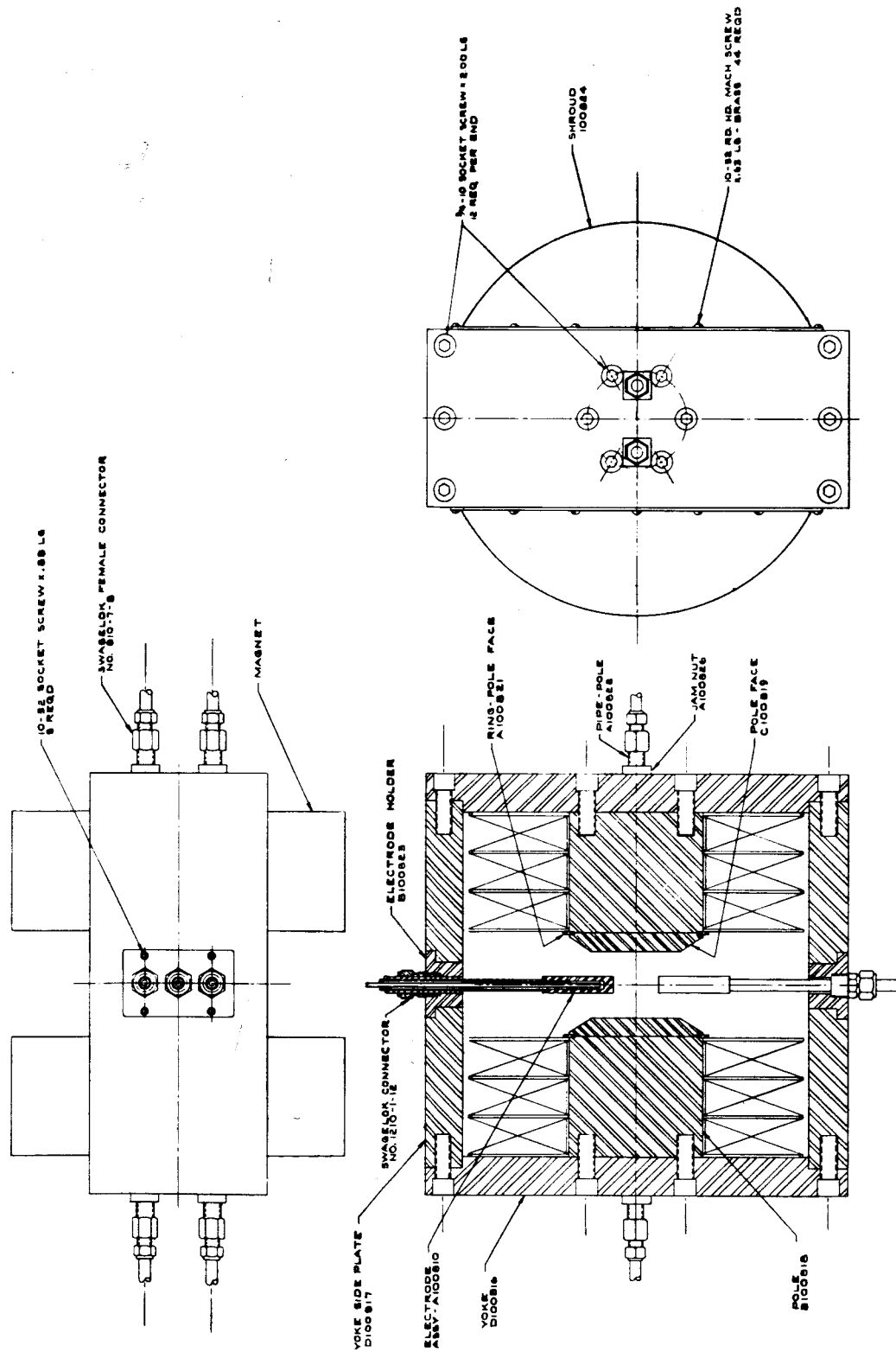
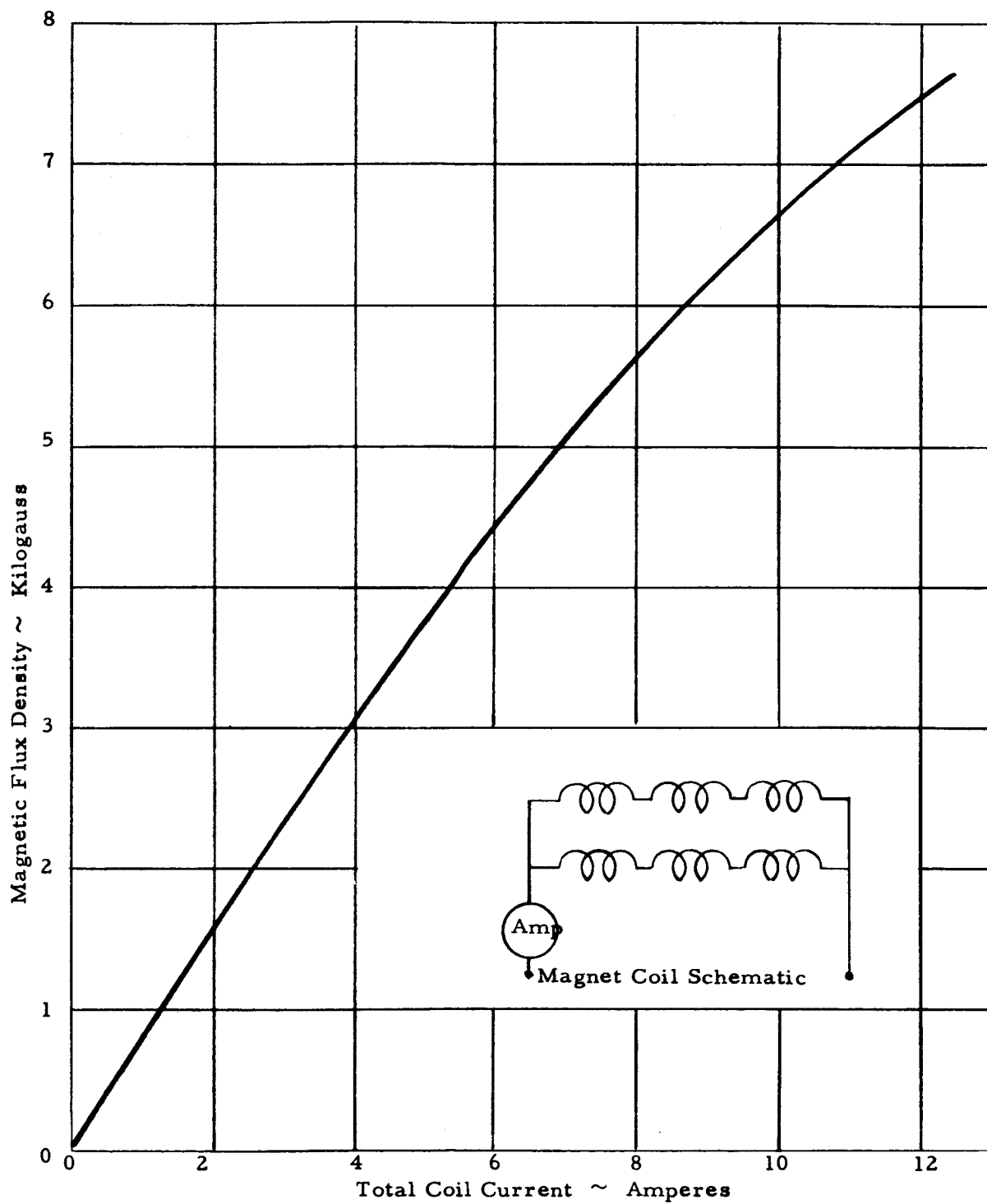


Figure 2. The Magnet Assembly



(B measured at center of 3" gap with coils in parallel)

Figure 3. Magnetic Flux Density as a Function of Current

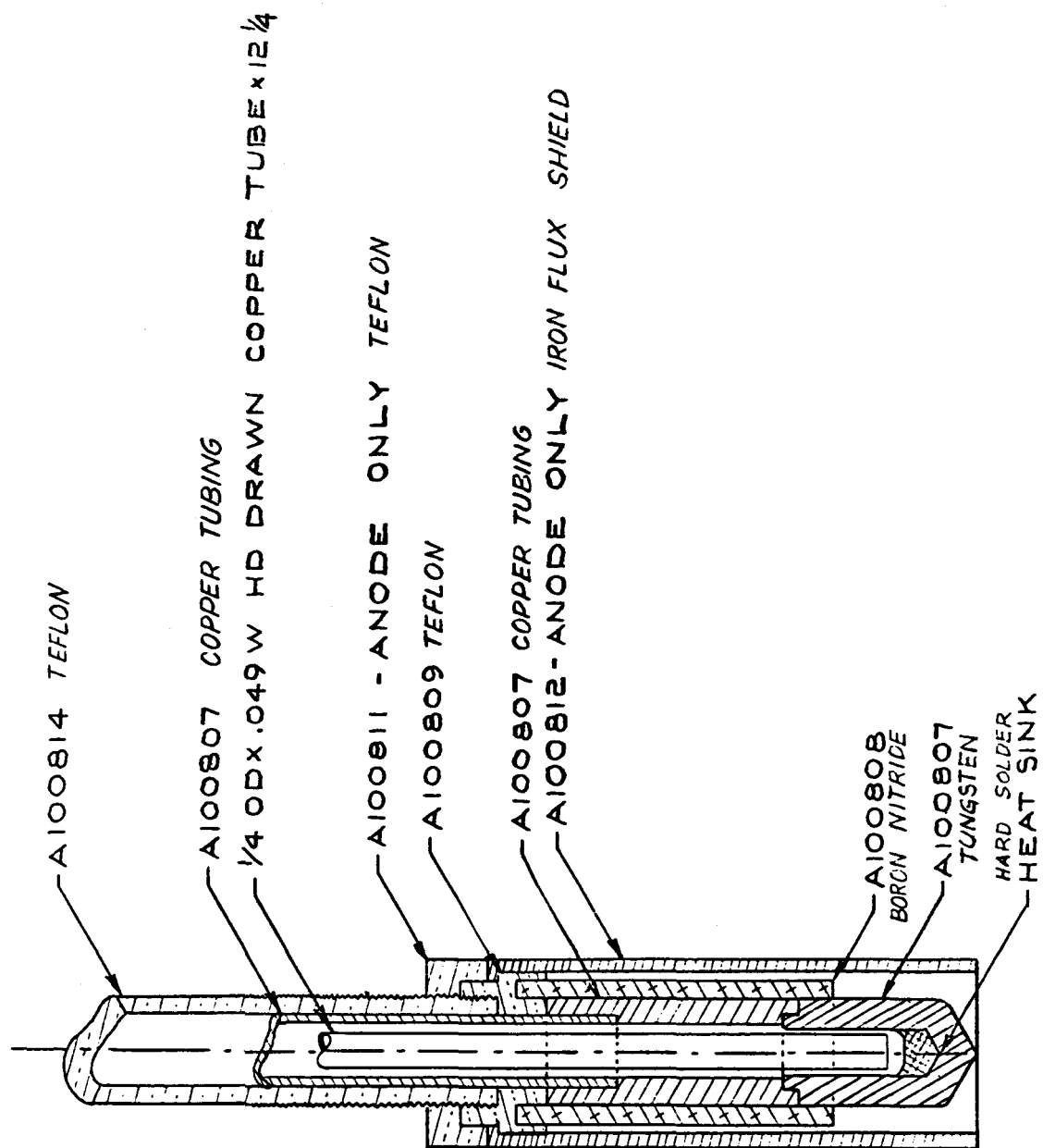


Figure 4. Electrode Assembly

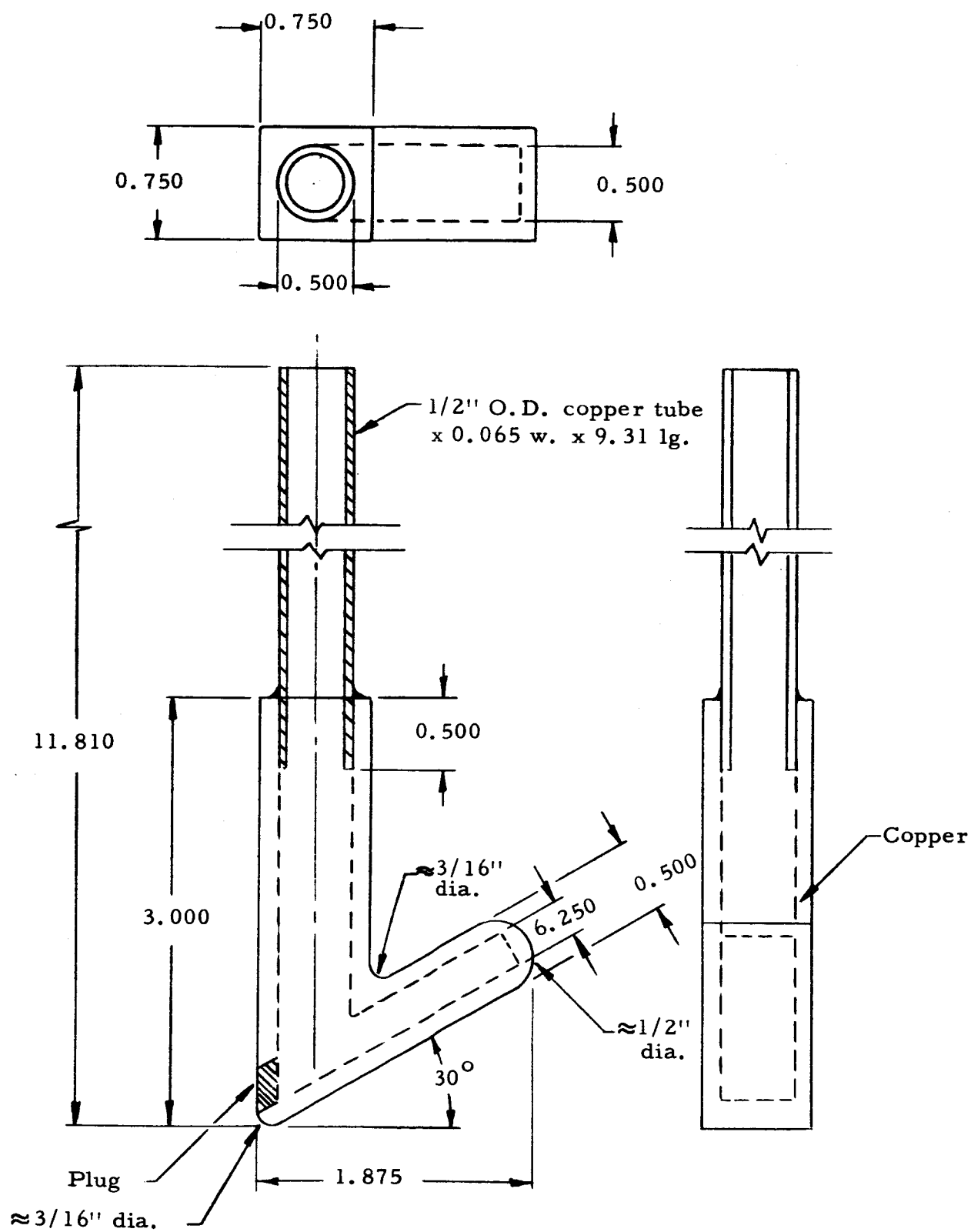


Figure 5. Copper Anode

Figure 6 shows two arc electrodes, one in an assembled condition and the other disassembled showing the component parts. The disassembled view displays the water-cooling cross, the tungsten electrode, a teflon insulator, the soft iron flux shield, the boron nitride insulator, and the connector fittings. To prevent the soft iron from exceeding its Curie point, the flux shield was wound with water-cooling coils. These are not shown in the photograph.

3. The Plasma Jet

The plasma generator used with the engine has been either a Thermal Dynamics Model U-50 or Model 40. The basic unit has been operated with a Thermal Dynamics laminar flow anode coupled to a settling chamber--Mach 3 de Laval nozzle combination or with an MHD Research, Inc. designed anode-nozzle unit.

The manufacturer states that with the laminar flow anode the plasma jet will operate over a power range from 5 - 30 KW with a flow rate of from 5 - 15 SCFM of argon. This corresponds to a mass flow rate of 0.07 - 0.21 gms/sec. It has been found that the plasma jet with this anode, but without the mixing chamber - de Laval nozzle combination, can be operated in air at one atmosphere with flow rates as low as 0.1 gm/sec of argon at a power level of the order of 10 KW. However, when operated in vacuum with the mixing chamber-nozzle combination it was not possible to operate the jet under stable conditions at flow rates below 0.5 gm/sec.

With the MHD Research, Inc. designed anode-nozzle (Figure 7) the plasma jet could be operated in vacuum at flow rates as low as 0.04 gm/sec with an input power of 20 KW (1000 amps., 20 volts). In the experimental discussions to follow, flow rates of 0.5 gm/sec of argon and above will be referred to as "high flow rates" and below 0.5 gm/sec will be referred to as "low flow rates".

4. Power Supplies

a. The Magnet Power Supply

The magnet power supply consists of a single phase 230 volt ac auto-transformer double ganged, an isolation transformer, a silicon rectifier bridge capable of 15 amps, and a 1000 microfarad filter capacitor. This supply is unregulated and can be adjusted continuously from 0 to 360 volts on open circuit. It is capable of delivering a continuous current of 12.5 amperes into any load between 0 and 24 ohms. Maximum continued output power is 3.5 KVA.

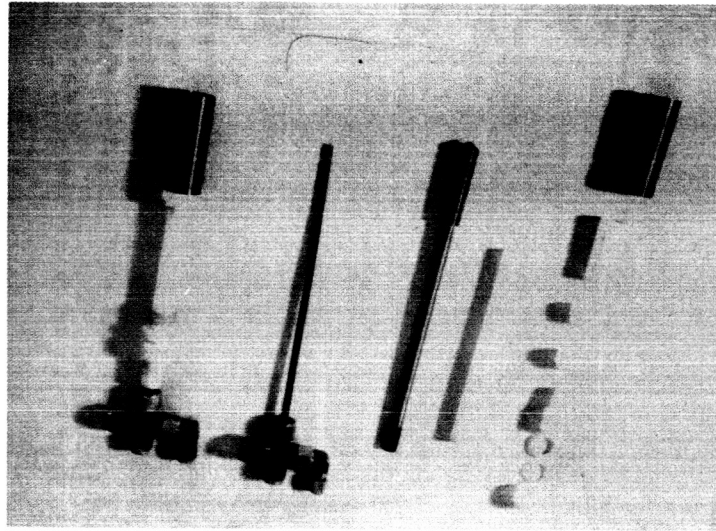


Figure 6. Photograph of Arc Electrodes

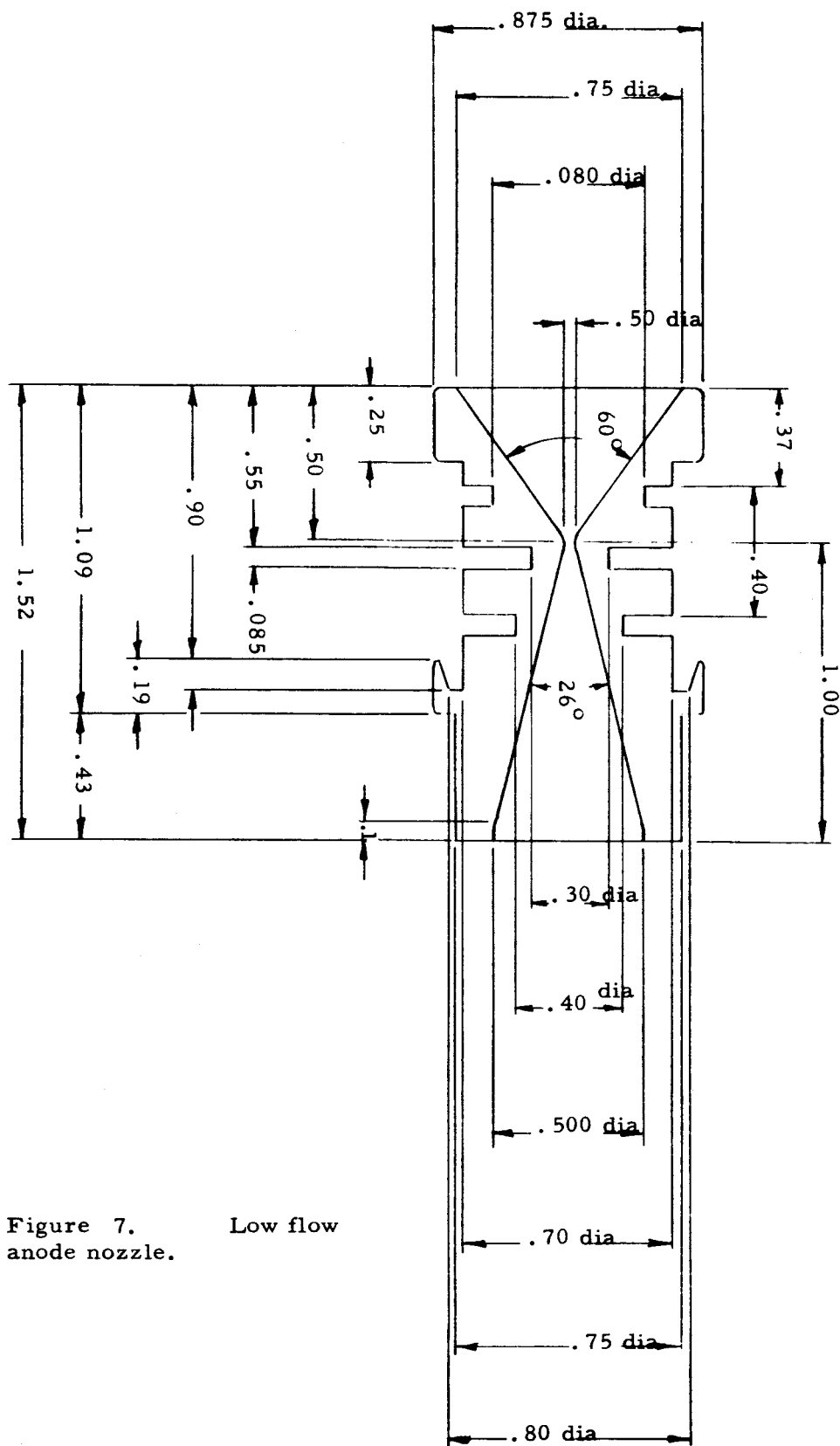


Figure 7. Low flow anode nozzle.

b. The Arc Power Supplies

The arc power supplies are 25 KW rectifiers manufactured by A. O. Smith. The rectifiers have connections for supplying three different open circuit voltages. The volt-ampere characteristics of these rectifiers are shown in Figure 8. Three of these rectifiers (A. O. Smith Model A6000 SR) are used in the cross-field accelerator experiments.

c. Plasma Jet Power Supply

Power is provided by a 40 KW, 160 OCV Miller welding rectifier.

C. THE VACUUM SYSTEM

The engine assembly is installed in a vacuum chamber measuring three feet in diameter and six feet in length. The chamber, shown in Figure 9, has a removable end plate and several access ports on the top and sides. The tank is evacuated by a Stokes Model 150-16 inch oil diffusion pump having a maximum pumping speed of 9500 cfm, and having an ultimate vacuum blankoff pressure of 8×10^{-5} millimeters of mercury. This pump is backed by Stokes Model 412-H mechanical pump having a pumping speed of 300 cfm, and capable of attaining an ultimate vacuum of 10^{-2} millimeters of mercury. A right angle pneumatically operated poppet valve is installed between the chamber and the oil diffusion pump. This valve is a Stokes Model 217-16 inch. The operation of this valve is controlled manually, or automatically by an adjustable thermocouple gauge controller set to close the valve at between 1.5 and 2 millimeters of mercury. Automatic control of this valve provides protection for the diffusion pump in case of a leak or other high pressure occurrence. The roughing and backing lines are six inches inside diameter and contain six inch gate-type valves. The chamber pressure and the pressure in the roughing and backing lines are monitored with 0 to 1000 micron thermocouple gauges. Thermocouple gauges having a range between 0 and 20 millimeters are installed in the engine working chamber and at the exit of the supersonic nozzle (if used). A Bourdon gauge having a range from 0 - 800 millimeters is used to monitor the pressure in mixing chamber downstream of the plasma jet nozzle.

The entire vacuum chamber is constructed of low carbon steel. Copper cooling coils are wound on the interior surface of the tank, and two water--cooled baffle plates are mounted on the end which connects to the diffusion pump. The engine assembly is mounted on a base plate which travels on rails mounted on the inside of the tank. The tray assembly and end dome form an integral unit which can be wheeled away from the tank to provide free access to the engine assembly. To make all portions of the vacuum chamber readily accessible, the pumping system is mounted in a pit sunk below floor

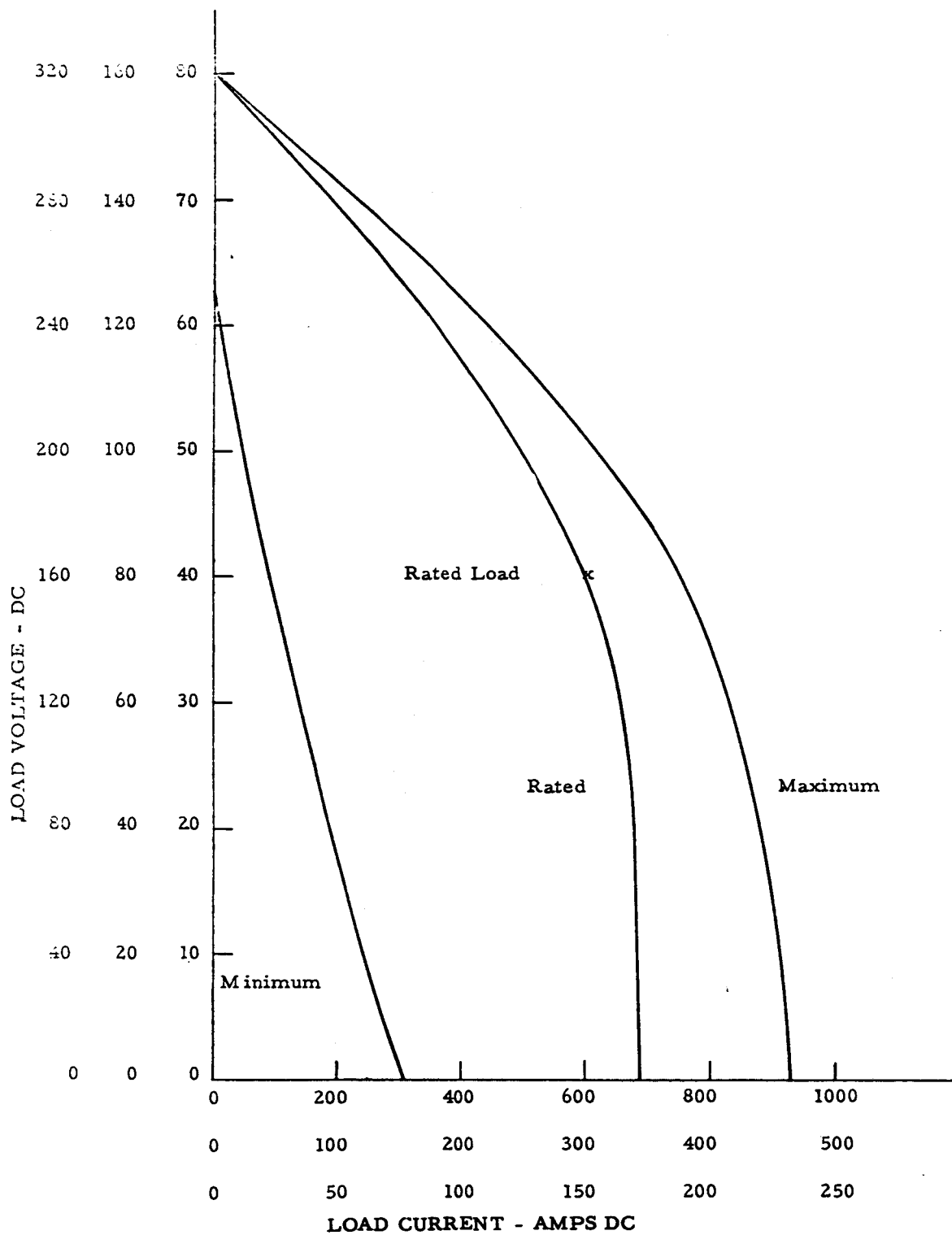


Figure 8. Volt-Ampere Characteristics of Arc Power Supply

Technical drawing of a vertical cylindrical vessel. The drawing shows a side view with a central vertical axis. The vessel has a cylindrical body, a hemispherical top, and a hemispherical bottom. Dimensions are indicated on the left: a total height of 90 and a section height of 48. A dashed line indicates an internal structure or a section cut. The top section shows a flange with four bolts. The middle section shows a larger flange with eight bolts. The bottom section shows a smaller flange with four bolts. A small circular feature is visible on the side of the vessel.

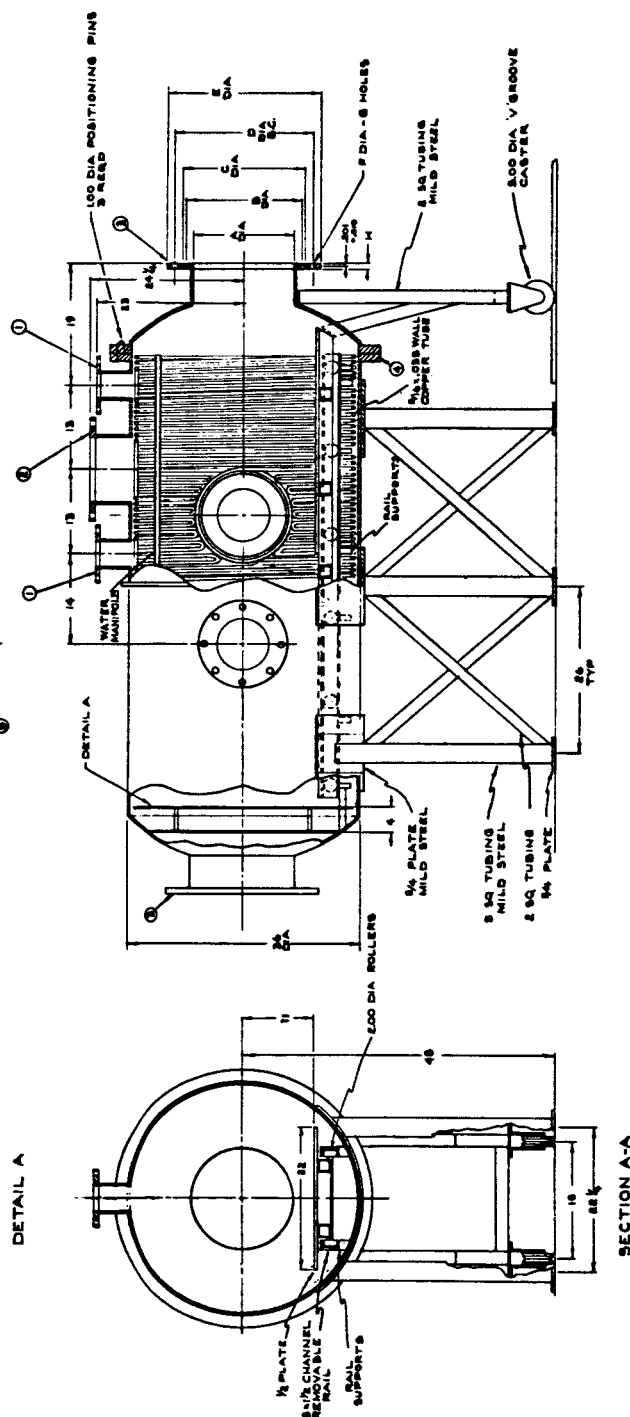


Figure 9. The Test Chamber

level. A layout of the vacuum chamber and pumping system is shown in Figure 10. This drawing shows the mechanical pump mounted at floor level. This pump is now located in the pit adjacent to the diffusion pump. Since the chamber is fabricated from low carbon steel and is consequently subject to erosion and oxidation, the interior of the chamber is coated with a film of vacuum pump oil. Figure 11 shows the partially opened vacuum chamber and a portion of the associated control panel. Figure 12 is a photograph of a portion of the pumping system and vacuum tank.

With the assembled engine in the vacuum chamber, and with all electrical and water systems "on", a chamber pressure of 100 microns mercury is readily achieved with the Stokes 412H mechanical pump. This situation applies when no gas is flowing into the plasma jet. With the Stokes Series 150-16 inch oil ejector pump operating, a chamber pressure below 10 microns is obtained. Starting with this base pressure, the chamber pressure versus throughput of argon in grams per second is shown in Figure 13. The curve marked "Indicated" is the pressure as read from a thermocouple gauge located on the top of the vacuum chamber. Since this gauge is calibrated to read the air pressure, a correction has to be made to obtain the true pressure in the chamber when argon is present. This figure indicates that a chamber pressure of the order of 80 microns can be maintained with a gas flow rate of 0.1 gram of argon per second. These curves also apply to room temperature data. With only the mechanical pump operating, plasma jet tests, at flow rates of the order of 0.04 grams per second, have been performed at chamber pressures of the order of two hundred microns. This would seem to imply that the gas is sufficiently cooled by the internal tank baffles so that the throughput closely approximates the room temperature data.

D. THE THRUST STAND

1. General Considerations

The measurement of the thrust of a $\vec{J} \times \vec{B}$ engine is not as straightforward as the one dimensional thrust measurements associated with a conventional jet or ion engine. The complication arises because of a second component of force due to the Hall deflection of the plasma beam. In the normal operation of the $\vec{J} \times \vec{B}$ engine the E field arc discharges in a vertical direction, while the B field is horizontal and perpendicular to the E field. The resulting Hall deflection lies in the vertical plane. As a result of the beam deflection there are two components of thrust, one in the direction perpendicular to the E and B fields, and one parallel to the E field. The magnitude of the vertical component of thrust is small compared to the weight of the engine itself and it is difficult to measure this component with sensitivity

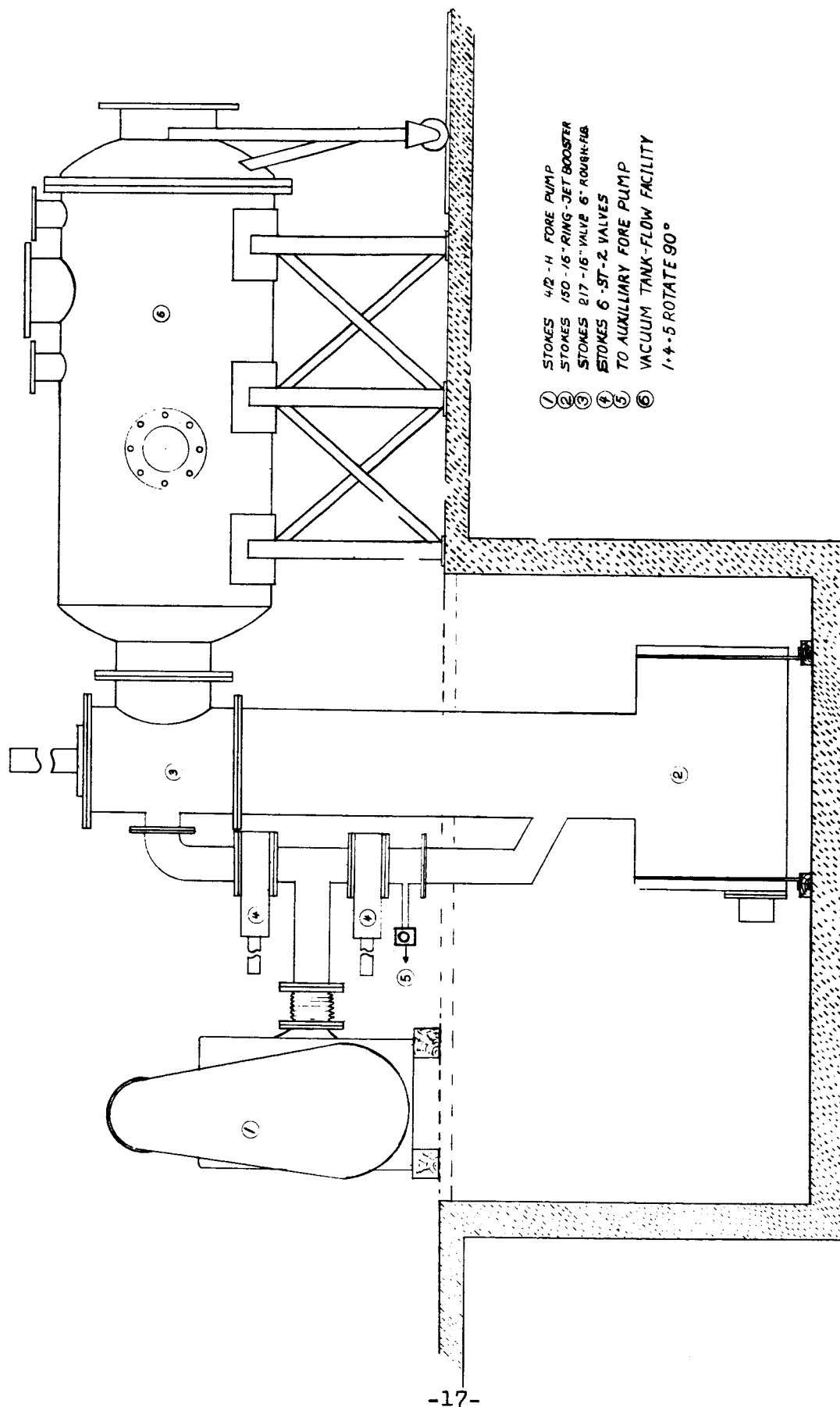


Figure 10. Layout of Vacuum System

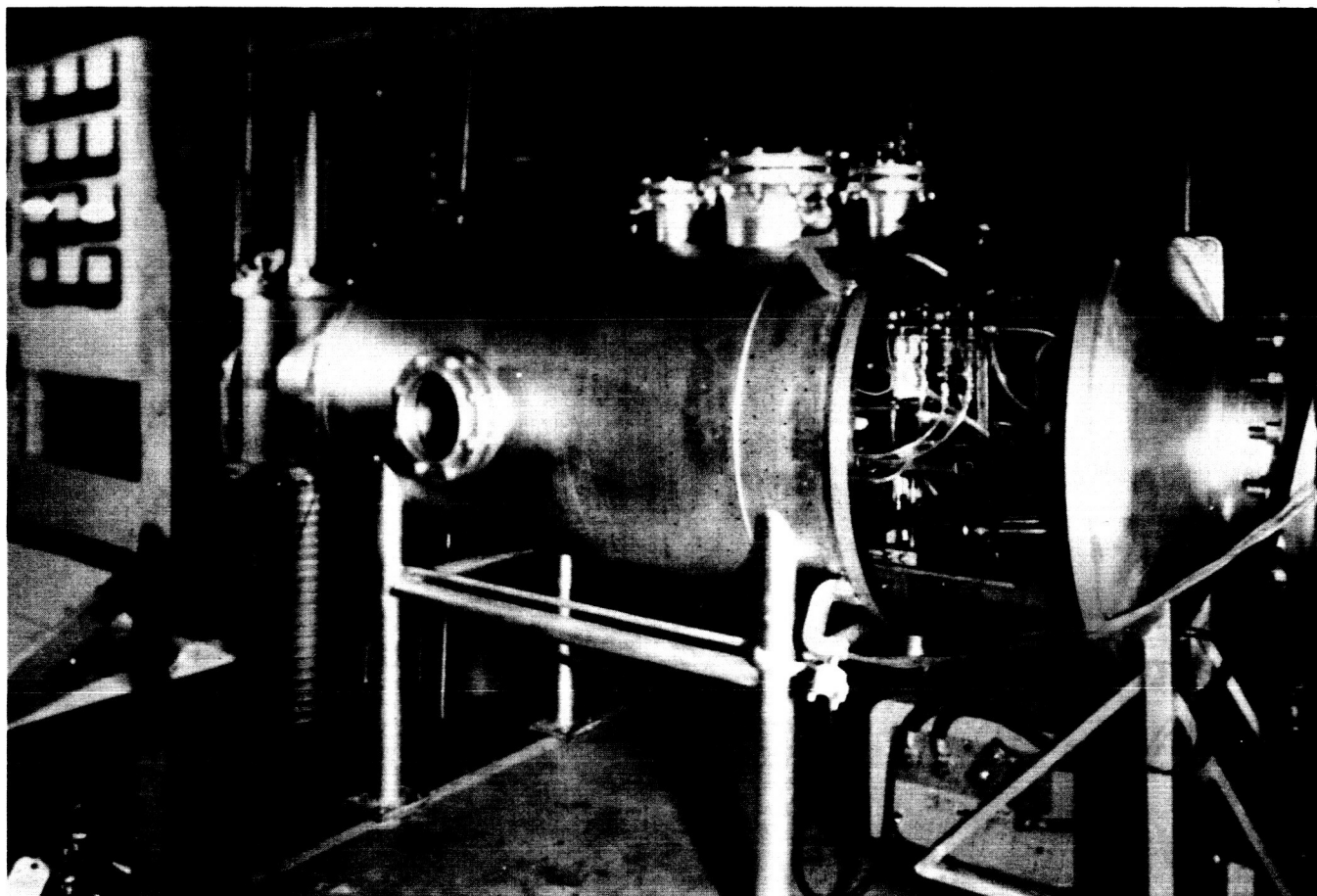


Figure 11. The Vacuum Chamber

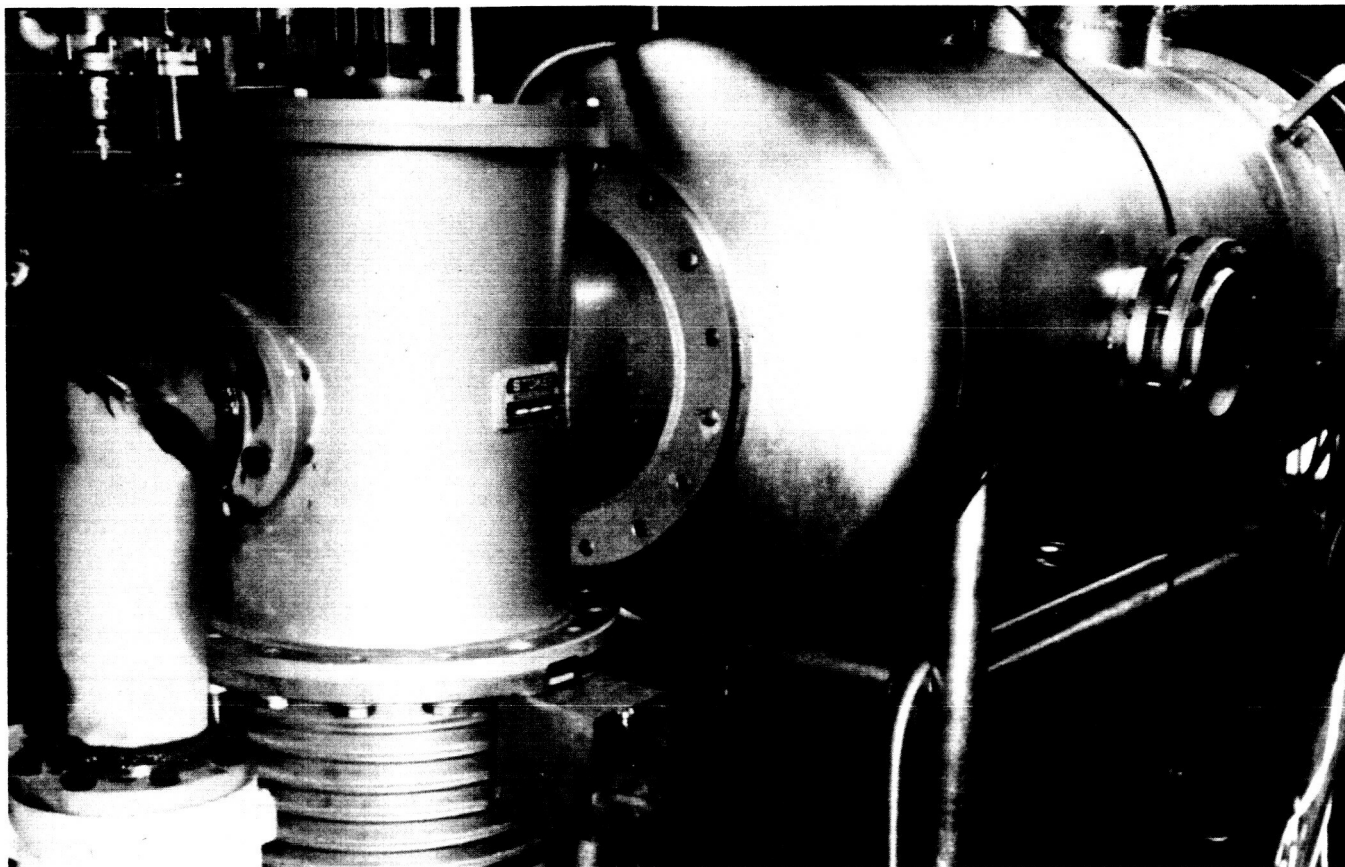


Figure 12. The Vacuum Chamber and Pumping System

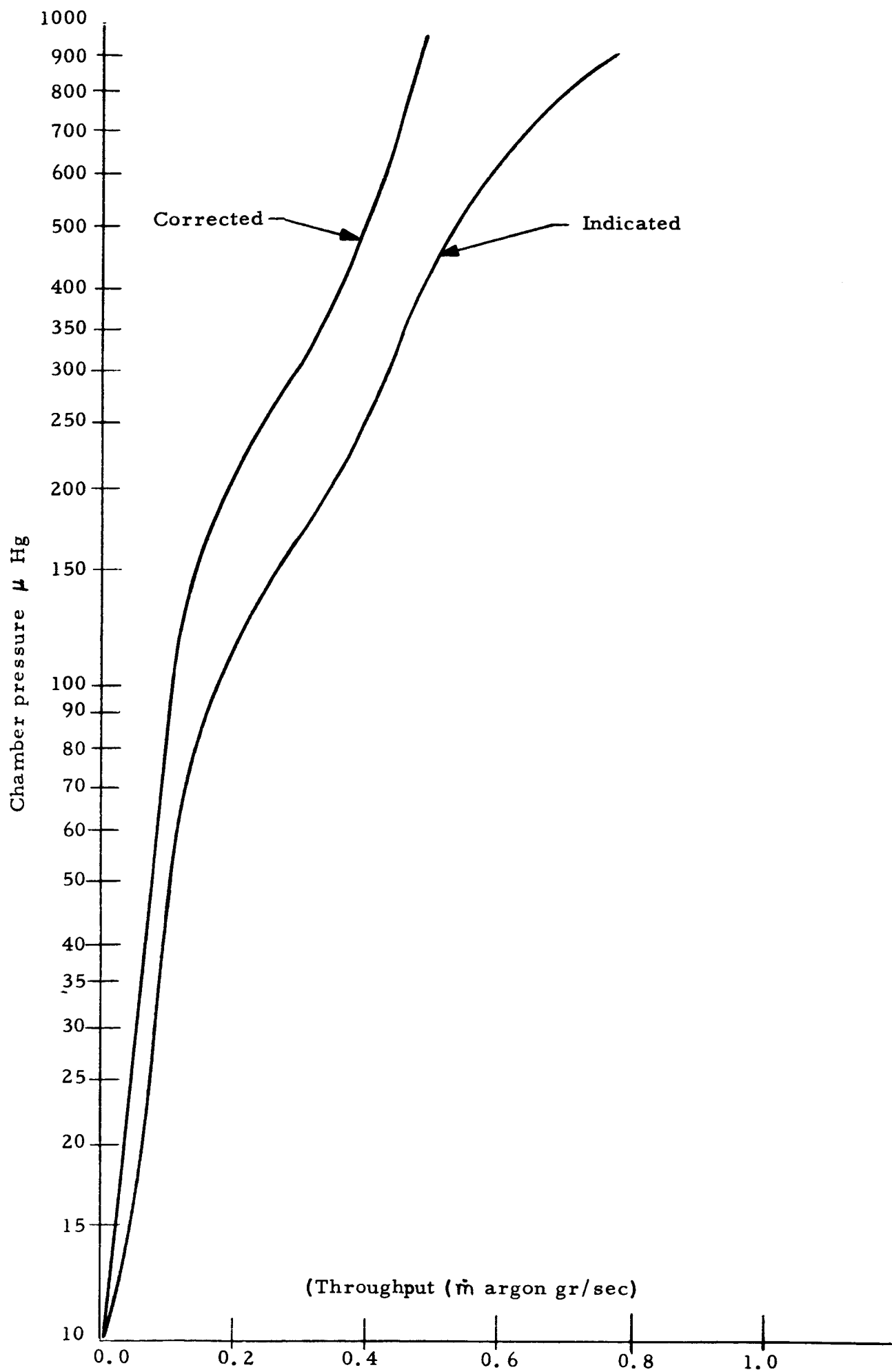


Figure 13.

Chamber pressure as a function of argon throughput

and accuracy. To measure both components of thrust with accuracy the engine is mounted on a thrust stand such that the E field arcs discharge in a horizontal plane. If we consider a right-handed coordinate system with the Z axis lying along the axis of the vacuum tank, the plasma will enter the field region along the Z axis, the magnetic field B will be oriented along the X axis, and the arc electrodes will lie in the YZ plane. The YZ plane defines the horizontal plane and the XZ plane the vertical plane. With the E and B fields off the plasma beam moves along the positive Z axis. Operation in this configuration reduces the problem to one of measuring a transverse and longitudinal force, both in a horizontal plane, without one of them being overpowered by the weight of the engine assembly. This technique simplifies the measurement problem but these perpendicular forces must be measured without crossfeed between the force gauges and without complications due to rotation of the engine. To eliminate crossfeed and rotation, a Cardan hinge dynamometer as shown in Figure 14 is utilized. The Cardan hinge is a thin flexure which acts as an essentially frictionless bearing. The thickness of the flexure is calculated to not only support the weight of the engine but to assist the force gauge in providing a restoring and righting force. The dynamometer then acts as though it were an inverted pendulum. The means for separating the two force components is provided by using two sets of Cardan hinges. One set of hinges is mounted parallel to the XZ plane and fixed between the engine at the top and a movable platform at the bottom. The force gauge mounted on the platform and bearing against the magnet measures the thrust in the Y direction. Also mounted to this platform are columns with cantilever supports mounted at the top. These cantilevers connect to a second pair of Cardan hinges lying in the XY plane and are fastened to the base plate inside the vacuum tank. The second force gauge is mounted on the base plate and bears against the movable platform. This gauge measures thrust in the Z direction. This arrangement allows complete freedom of motion of the engine in a horizontal plane, prevents crossfeed of force data between the two gauges and prevents rotation of the engine assembly.

Since the dynamometer is quite sensitive it is necessary to provide some means of preventing measurement interference caused by cooling water and electrical power connections. Since the magnetic force on a current loop is always such as to expand the current carrying circuit, the leads carrying current to the electrodes will tend to stiffen and this force will be indicated by the dynamometer. To prevent this transmittal of force mercury pots are used for electrical connections. The leads from the engine assembly are solid rods, the ends of which are immersed in pots of mercury which complete the circuit. This technique removes restraints on the engine movement and prevents transmission of any extraneous forces from the electrical leads to the dynamometer. A dynamic balancing principle is used to prevent forces or

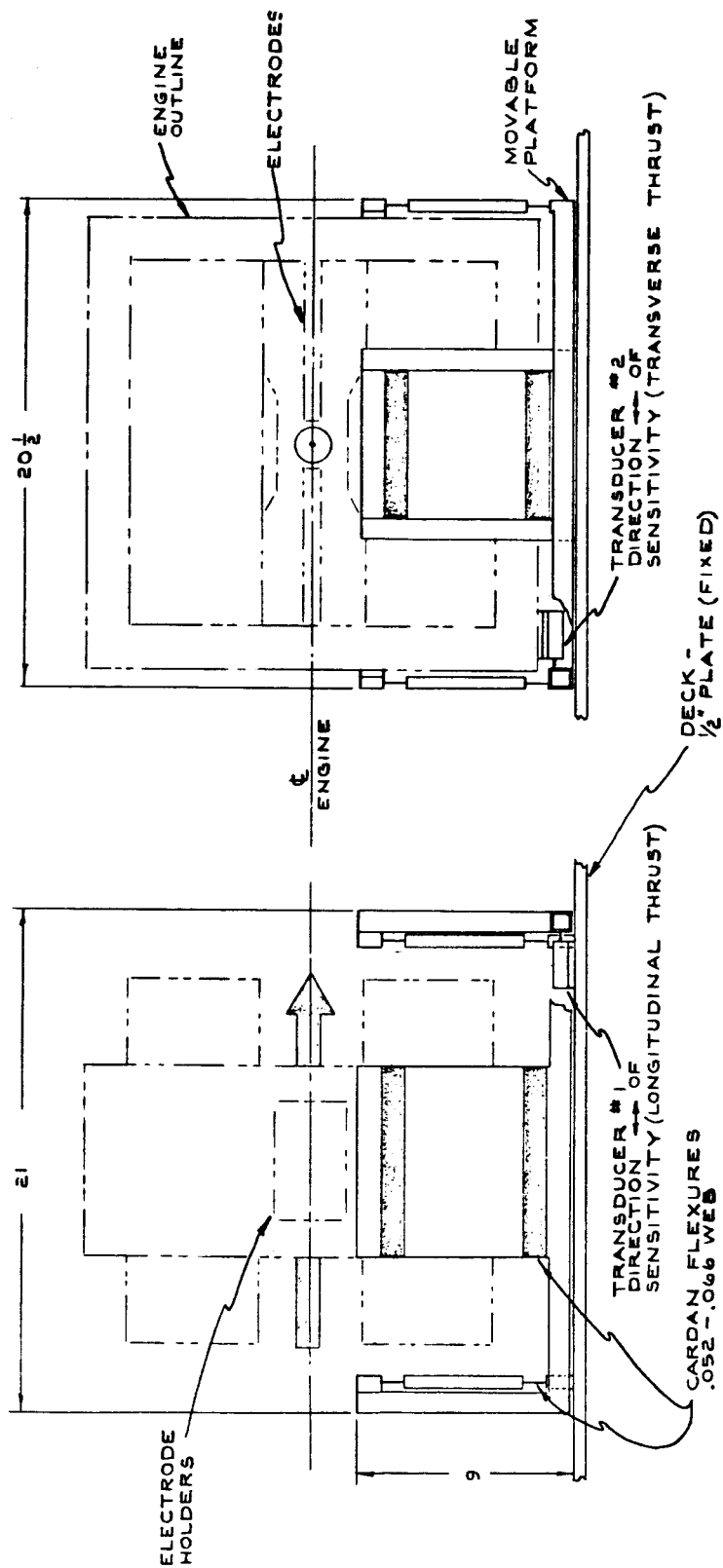


Figure 14. The Dynamometer

restraints due to cooling water pressure from being transmitted to the dynamometer. The water leads are flexible to prevent restraints and are routed so as to balance input and output pressure on both sides. An analysis of the system is presented in Appendix II.

2. Calibration of the Dynamometer

To calibrate the dynamometer, an equal-arm right-angle balance was constructed as shown in Figure 15. Four 100 gram weights were supported on a four inch horizontal arm. By means of a pulley system, the weights may be successively removed from, or replaced on the arm, thus giving thrust increments of 400, 300, 200, and 100 grams to the magnet. The force is transmitted to the magnet through a vertical arm having an adjustable screw member which bears upon the movable carriage of the dynamometer. This serves to calibrate the dynamometer in the longitudinal direction. A similar arrangement is used to calibrate in the transverse direction. The 400 gram weight produces a horizontal displacement of approximately 0.00065 inches which is translated by a "Statham", unbonded strain gauge (32 ounce maximum, 0.0015 inch displacement) as an electrical signal, to a recording oscillograph. This calibration may be performed in vacuum before and after engine operation. In addition, a solenoid has been installed, the armature of which bears on the movable carriage of the dynamometer when the solenoid is activated. By adjusting the current in the solenoid a calibrated deflection can be given to check the operation of the system while under vacuum.

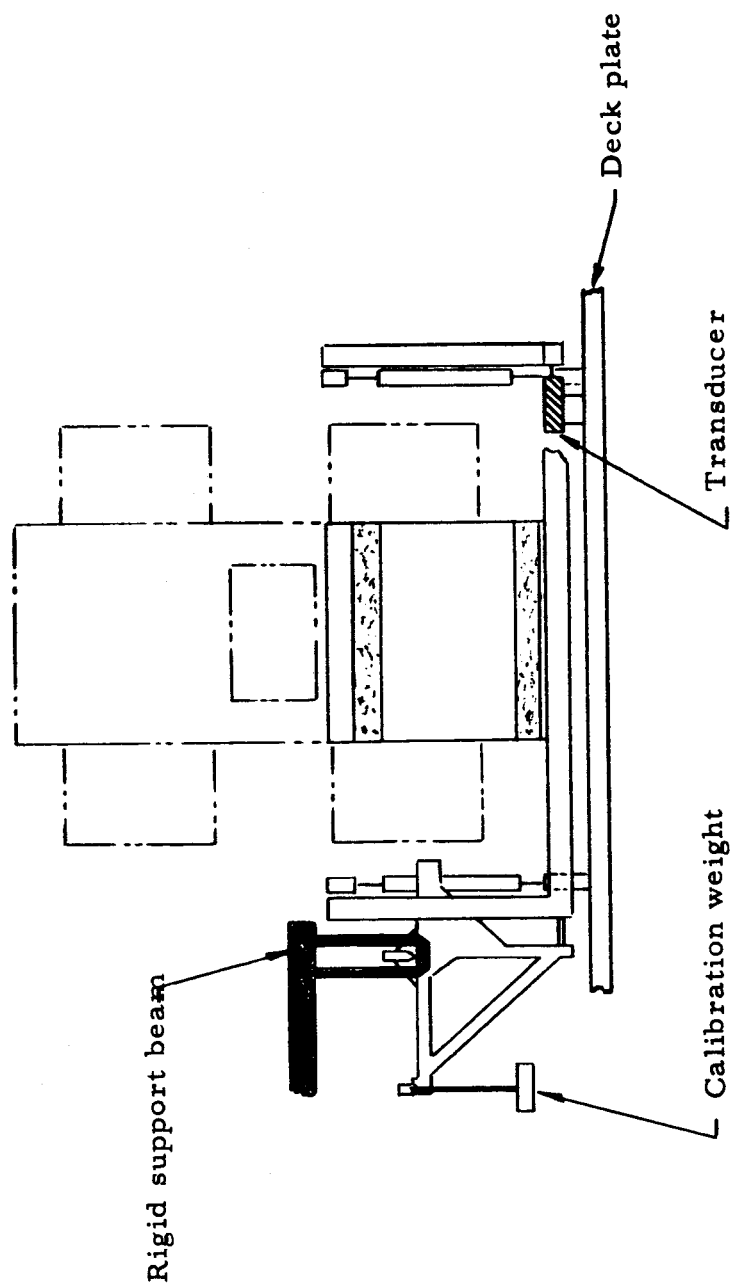


Figure 15. Calibration system.

E. INSTRUMENTATION

1. Instrumentation Organization

Data instrumentation is classified under the following headings: (1) data that is monitored only; (2) data that is monitored and recorded by camera; and (3) data that is recorded by an oscillograph (Figure 16).

Information classified as "monitored only" deals with water pressures and flows and other items, that once set, do not change during operation. These instruments are located on a separate panel above the control panel.

Information classified as "monitored and recorded by camera" deals with variables in the system pertaining to engine operation. These instruments are located on a separate panel also above the control panel. A running time clock is located on this panel so that all information can be time-correlated. A moving picture camera can be controlled to take pictures of this panel at any time during operation. It is not necessary for the operator to come between the camera and this instrumentation panel during operation of the system.

Information classified as "recorded by oscillograph" deals with the engine thrust data. Power to the B field and E field are recorded along with transverse and longitudinal thrust of the engine. These signals are time-correlated with all other events of the system by signals from the same clock that is located on the "recorded by camera" panel.

The vacuum instrumentation panel is provided with: (1) a 0 - 800 mm Hg manometer installed to read the supersonic mixing chamber pressure; (2) a 0 - 50 mm Hg manometer installed to read nozzle exit pressure; (3) a three station 0 - 1000 Hg thermocouple gauge reading environmental chamber, diffusion pump inlet and backing-roughing line pressures; and (4) a 0 - 20 mm Hg thermocouple gauge installed to read pressure inside the engine. If this environment is too severe for a T. C. gauge the pressure can be read on the 0 - 50 mm Hg manometer with the addition of appropriate valving. These gauges are in addition to the 0 - 20 mm Hg gauge used to control the closing of the 16 inch valve in the event of a high pressure excursion.

The cooling water system consists of two separate sections. A distilled water heat exchanger is used to cool the plasma jet and the E field electrodes. A second heat exchanger using zeolite softened tap water is used to cool the vacuum pumps, the distilled water heat exchanger, the vacuum tank cooling coils and baffles and all non-electrical components of the engine assembly and dynamometer.

2. Control Panel

The control panel (Figure 17) is designed to allow the operator to easily reach all controls. It is divided into seven major divisions as shown in the control panel illustration. A schematic diagram is drawn on the control panels of each major portion of the system. The pilot lights and control switches are located in the correct positions on those diagrams to increase ease of operation.

The warning panel has seven lights and a bell that indicate "unsafe to operate" conditions. If any one or more of these lights are on, interlocking switches and relays will prevent the system from being operated. In addition, interlocking switches and relays in almost all cases prevent the operation of controls out of proper sequence.

Figure 18 is a photograph of the controls and instrumentation console. Starting from the left-hand side of the picture the first panel contains the recording oscillograph; below it is the control panel for operating the distilled and soft water pumps. Next, to the right, is the vacuum control panel controlling the mechanical, diffusion pump and the vacuum instrumentation. The third panel from the left contains the warning lights indicating lack of water pressure or flow, high tank pressure, and other circumstances, deleterious to the running of the tests. Below the warning panel, are the buttons and controls to provide gas flow and r.f. to the plasma jet to properly center the plasma jet electrodes. This panel also contains the control Variac for the magnet power supply. The next panel to the right is the arc gas handling and metering panel and the control panel for the E field electrodes. The next panel to the right contains the vacuum instrumentation read out, the cooling water flow, the ΔT (inlet and outlet temperature difference) panel as well as the controls for the plasma head. The last panel contains the voltmeters and ammeters for the plasma head, the E field arcs, and the magnet and the microammeters monitoring the thrust in both the transverse and longitudinal directions. Not shown on the photograph is a motion picture camera regulated for continuous or single frame operation, focused to photograph the last three panels on the right for continuous or semi-automatic data recording.

3. Flow Meter

The method to be used to measure the flow rate of the cooling water is illustrated in Figure 19. The water entering the meter at a temperature T_1 passes a heater H, which is energized by the source S, and emerges with a higher temperature T_2 . If the specific heat is constant

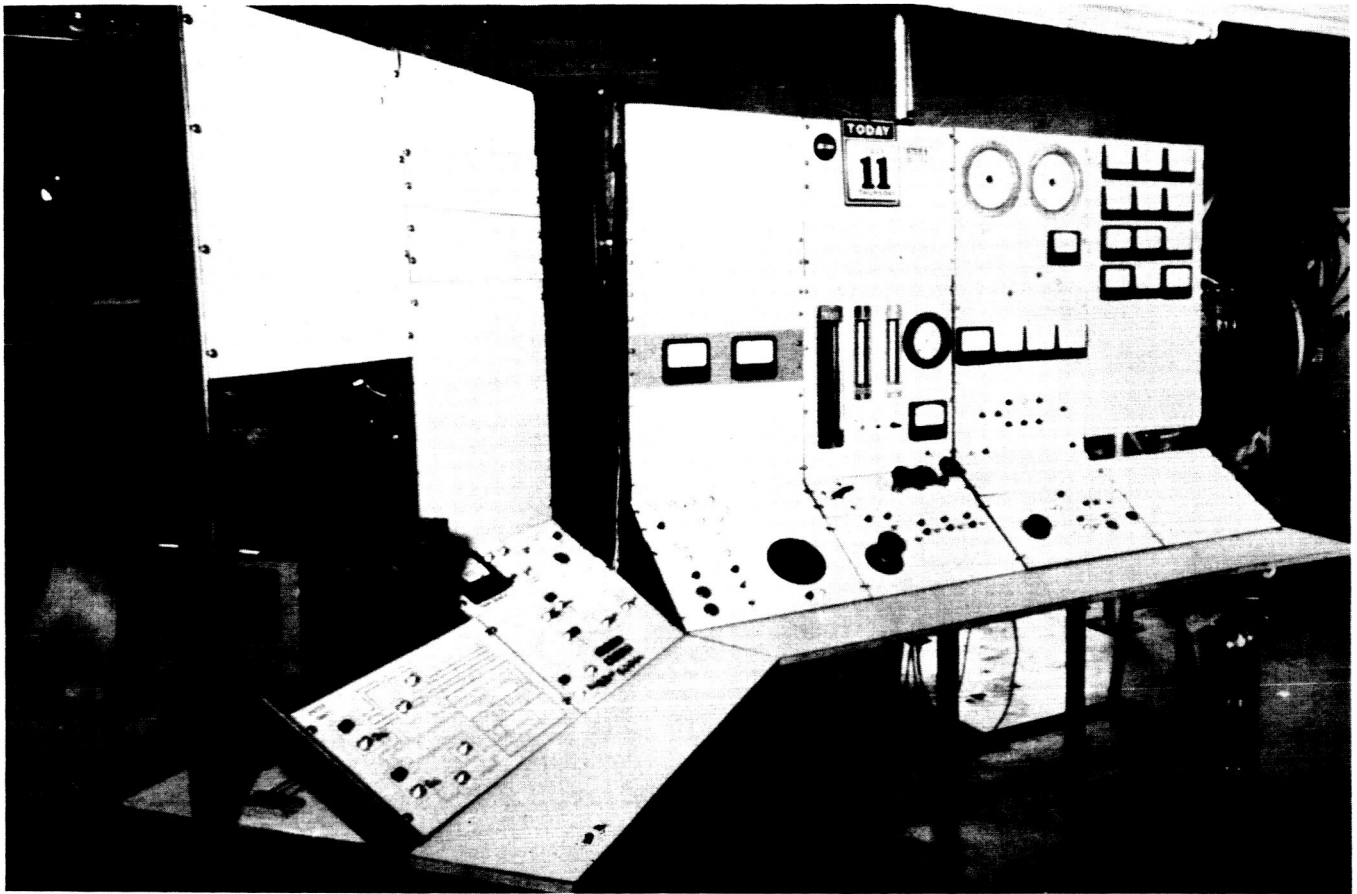


Figure 18. Controls and Instrumentation Console

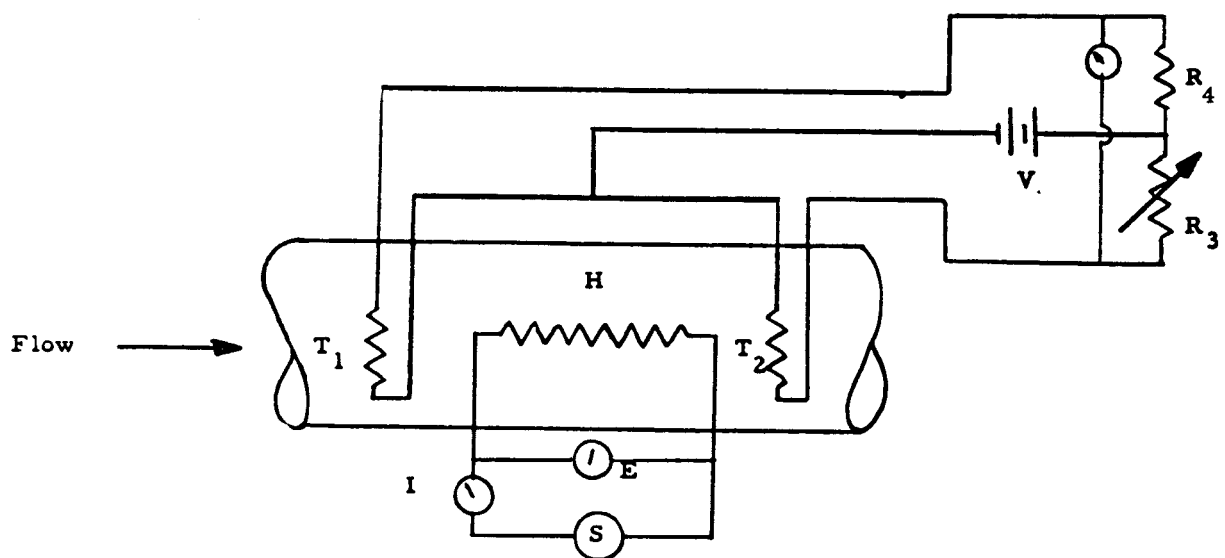


Figure 19. Schematic of Thermistor Flow Meter

which for water is approximately true, the flow rate F can be determined from

$$F = \frac{PC}{C_p(T_2 - T_1)}$$

where P is the electric power required for the heater, C is the mechanical-caloric equivalent, and C_p the specific heat of the water.

The temperature difference $T_2 - T_1$ is measured by determining the difference in resistance of two thermistor elements placed in the flow. The difference in resistance of the two thermistors is determined by connecting them in two adjacent arms of a Wheatstone bridge which is balanced when the thermistors are at the same temperature. The temperature difference $T_1 - T_2$ is then calculated from the microammeter reading in the bridge when the bridge is unbalanced due to the change in resistance of the downstream thermistor.

The thermistors used in these meters were Fenwal GB 32 J 1. The thermistor resistance as a function of temperature is shown in Figure 20. At 20°C $\frac{dR}{dT} = -95 \Omega / ^\circ\text{C}$ and at 30°C $\frac{dR}{dT} = -64 \Omega / ^\circ\text{C}$. If R_1 and R_2 are the resistances of the thermistors at temperatures T_1 and T_2 , then the current through the microammeter is

$$I_b = \frac{V(R_1 R_3 - R_2 R_4)}{R_4 R_1 (R_2 + R_3) + R_2 R_3 (R_1 + R_4) + R_g (R_2 + R_3)(R_1 + R_4)}$$

where R_g is the meter resistance, and R_3 and R_4 are as shown on Figure 19.

At 30° the resistance $R_1 \approx 1645$ ohms. For a 0.1°C rise in temperature $R_2 \approx 1651$ ohms. With $R_g = 0$ and $R_3 = R_4 = 6000$ ohms, and $V = 6$ volts

$$I_b \approx 1 \mu \text{ amp.}$$

In the actual meters, a portion of the cooling water flow was bypassed through a stainless steel heating coil. Figure 21 shows the meter calibration curve obtained with heater powers of 1.14, 2.08, and 3.20 watts, with $R_3 = R_4 = 6000$ ohms, and for 1.14 watts with $R_3 = R_4 = 4000$ ohms.

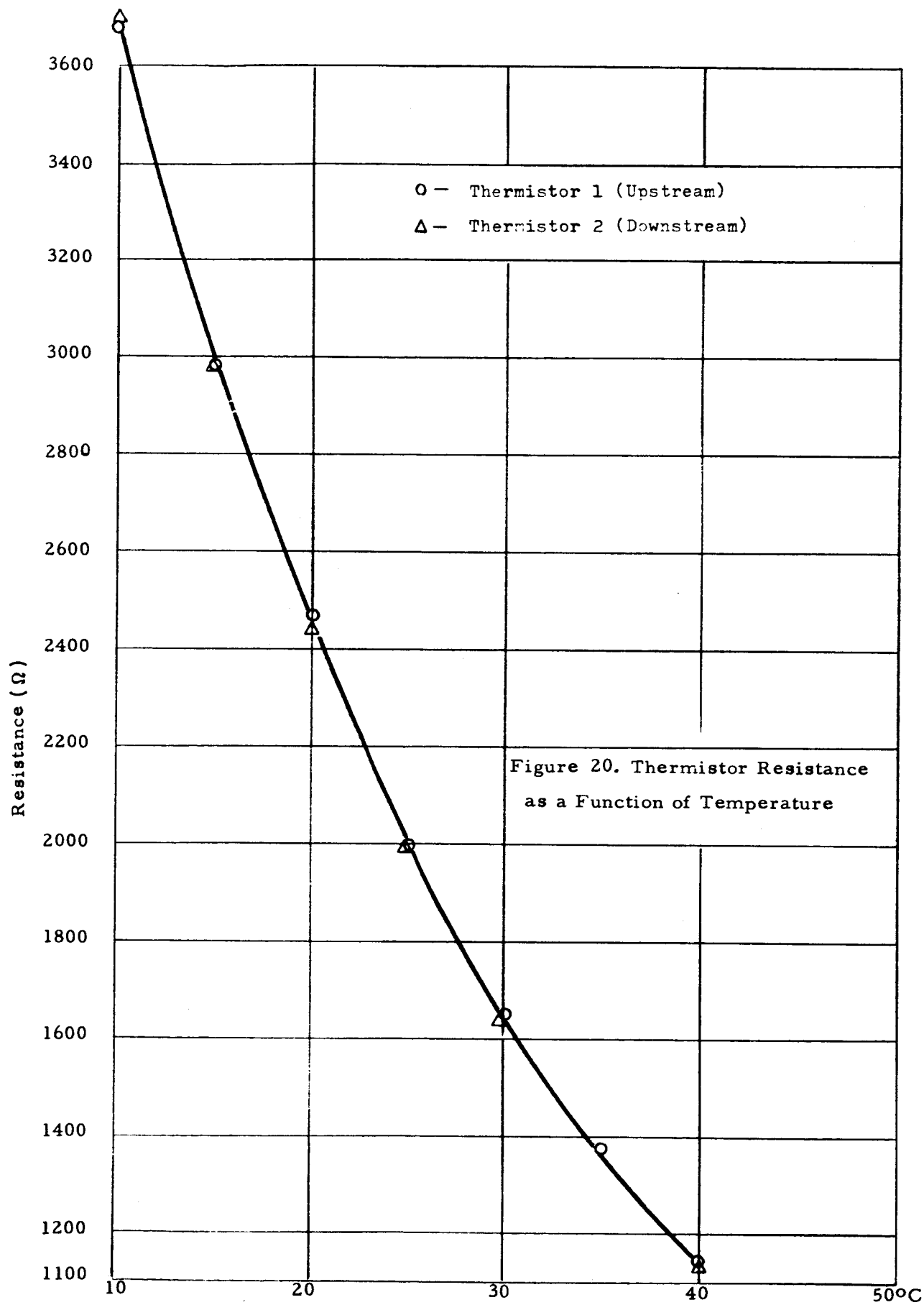


Figure 20. Thermistor Resistance
as a Function of Temperature

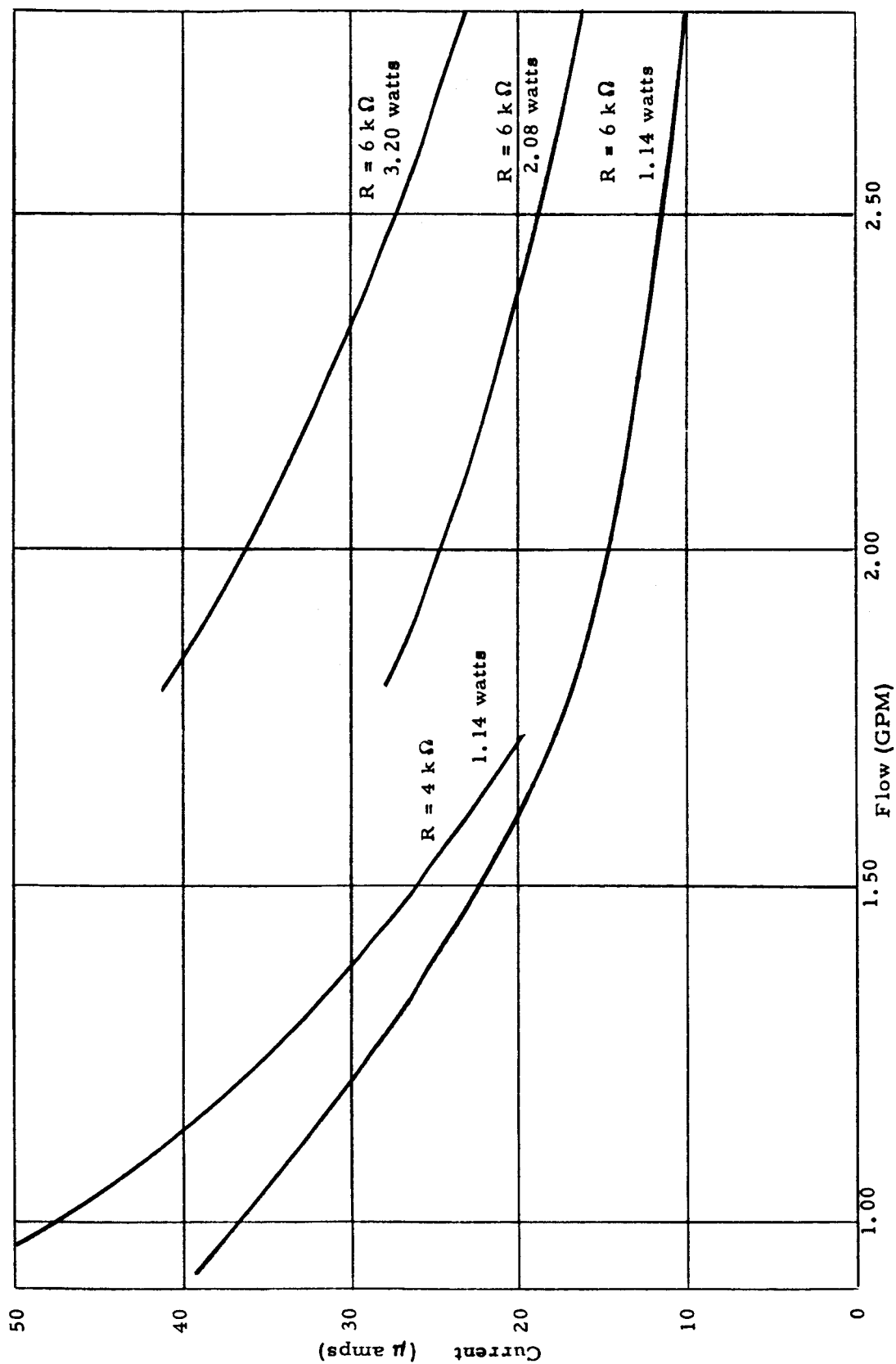


Figure 21. Meter Current as a Function of Water Flow

F. THE ENGINE ASSEMBLY

Figure 22 shows a partially assembled engine without the plasma jet and with only one set of cathodes. The photograph shows the electrode housing and the lucite mercury cups. The brackets shown hold water-cooling manifolds. The electrodes are without the boron nitride sheaths and the magnet pole faces are without the quartz protective faces. Figure 23 depicts the completely assembled engine mounted on the dynamometer which in turn is mounted on the base plate of the removable tray. The electrode leads are immersed in the mercury pots and the electrodes are sheathed in boron nitride protective sheaths. The figure shows both the longitudinal and transverse Cardan hinges. The apparatus in the left forward corner is for thrust Calibration.

Figure 24 is a view looking upstream toward the plasma jet and supersonic nozzle. The quartz plates protecting the upper and lower magnet faces are spaced with magnesium oxide spacers. The three pairs of tungsten electrodes shown are sheathed to within 1 inch of the tip with boron nitride. The electrodes are spaced successively $7/8$, 1, and $1-1/8$ inches apart. The spacing along the channel is $1-1/2$ inches on the centers of each electrode.

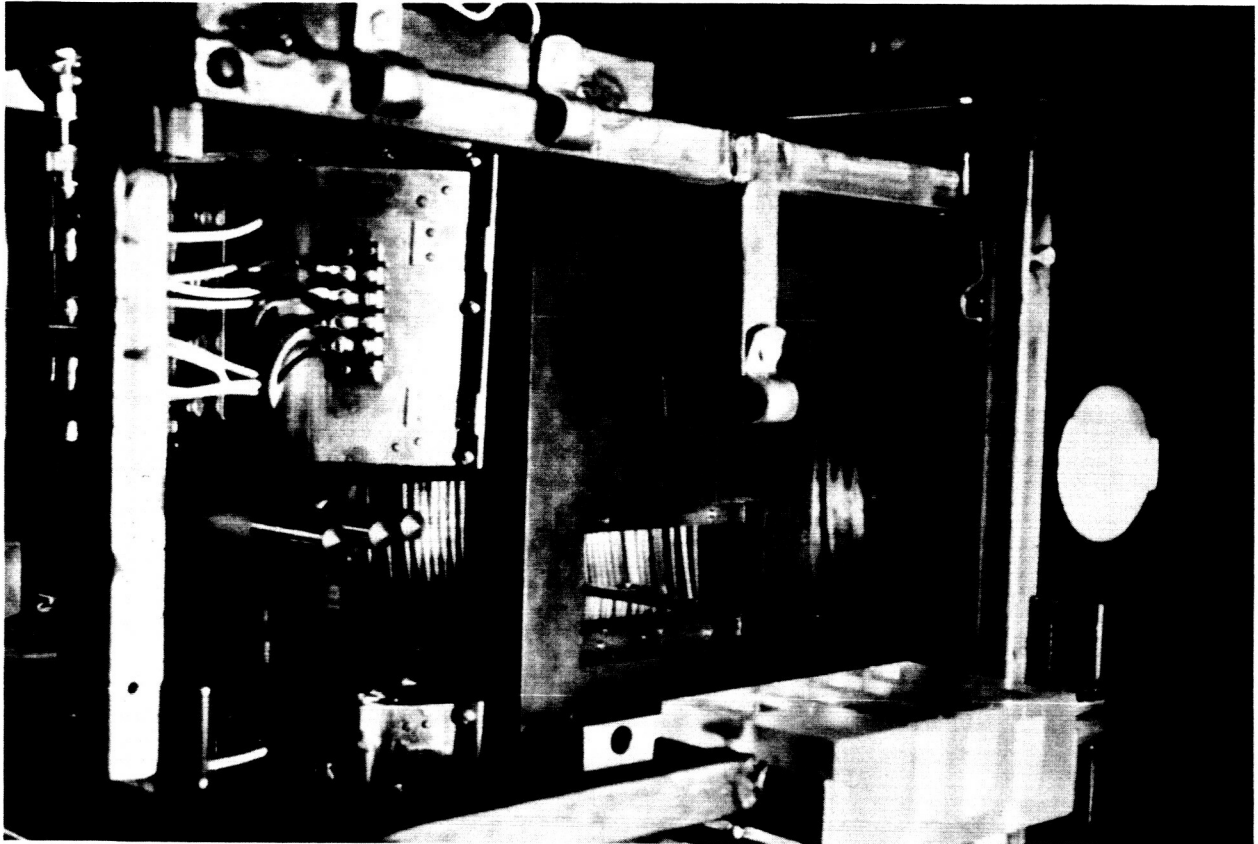


Figure 22. Partially assembled engine

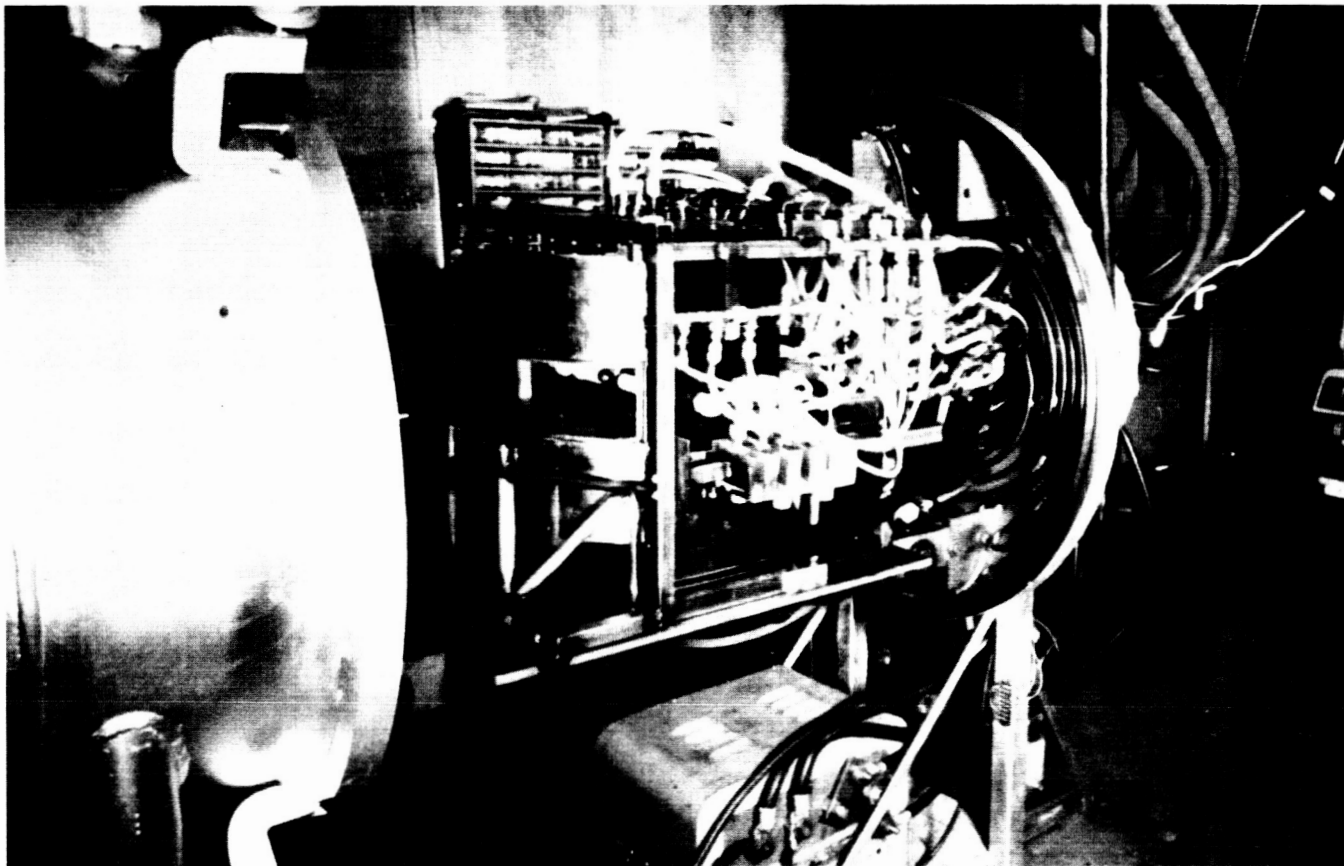


Figure 23. Complete Engine Assembly



Figure 24. Crossed field region of the accelerator
Anodes at right

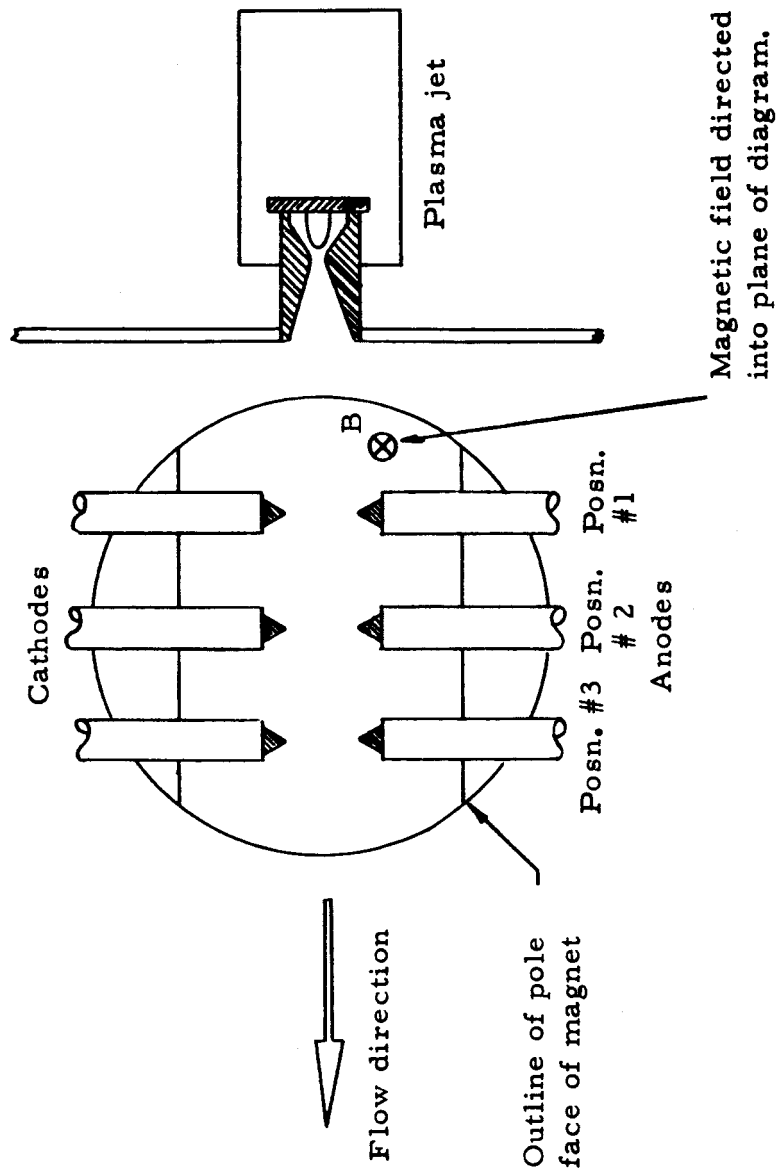
III. ENGINE PERFORMANCE

A. HIGH GAS FLOW EXPERIMENTS

The Thermal Dynamics model U-50 plasma jet with Thermal Dynamic's laminar flow nozzle (Section II, B 3) was operated in air without the mixing chamber and deLaval nozzle with argon at flow rates from 0.1 - 0.5 gm/sec with a mixture of helium at flow rates ranging from 0 to 0.7 standard cubic feet per minute. Over these ranges of operating conditions the voltage and current characteristics of the plasma jet remained essentially the same as they were for the argon flow only. That is, the additional amount of helium added to the flow had very little effect on the operating characteristics of the plasma jet within the ranges stated. A similar experiment was performed with the plasma jet mounted to the engine in the vacuum chamber. As stated in Section II, B 3, it was not possible to operate the plasma jet at argon flow rates below 0.5 gm/sec, but above this flow rate the additional helium had very little effect on the voltage-current characteristics of the jet. No argon-helium mixtures were used with the cross fields operating.

Initial experiments were performed with the tungsten electrodes with magnetic flux shields mounted on the anodes only. It was found that stable arc operation could be obtained both with and without the magnetic field operating but that the downstream edges of the flux shields were quickly eroded. This caused a rapid burn-through of the cooling coils mounted around the flux shields with resultant water leaks. In any case, the soft iron shields were heated above the Curie point and no longer served their purpose as magnetic flux shields. No meaningful thrust measurements were obtained during the series of experiments other than those associated with the plasma jet operating only. At a flow rate of 0.8 gm/sec the longitudinal thrust was of the order of 70 grams with the plasma jet operating at approximately 9 KW (300 amps, 30 volts).

A second series of experiments was performed using a single electrode pair only mounted in the No. 2 position with reference to Figure 25. In these experiments the cathode consisted of a single tungsten electrode as previously described while the anode, as shown in Figure 5, was fabricated of copper with a water-cooled portion extending approximately 1-1/4 inches downstream and tapering at an angle of 20 degrees from the axis of the accelerator. The plasma jet in these tests was operated at approximately 9 KW with 0.8 gm/sec argon. The arc operated at



Accelerator electrode positions

Figure 25

150 amps and at a voltage ranging from approximately 132 - 200 volts depending on the magnetic field strength applied. At a magnetic field strength of approximately 1000 gauss there was a Hall deflection of the jet of approximately 20 degrees with a 5 - 10 degree downward deflection on the cathode side. The arc appeared to strike on the downstream side of the anode with no definite point of attachment on the cathode. No thrust was recorded above that generated by the plasma jet only; neither with the arc operating alone nor with the arc operating in magnetic fields ranging from 0 - 2000 gauss.

In a third series of experiments a single pair of electrodes was placed in a staggered position with the cathode being in the number two position, with reference to Figure 25, and the anode being mounted in the number one position, nearest the plasma jet end of the engine. The anode in this case had a tungsten tip as previously described and both the anode and cathode were sheathed in quartz to within approximately 3/4 inch of the tapered end. The longitudinal spacing of the electrodes was 1-1/2 inches on center, and the lateral spacing was approximately 7/8 inch. The plasma jet was operated with argon at 26 volts and 300 amps with the flow rate of 0.8 gm/sec. The pressure in the main vacuum chamber throughout the run was 2.5 torr. Arc operation was very stable up to field strengths of 2000 gauss. The following Table I shows the voltage characteristics of the arc for various magnetic field strengths.

TABLE I

Chamber Pressure - 2.5 torr
 Plasma Jet: Current - 300 amps, Voltage - 26 volts
 Gas Flow Rate: 0.8 gm/sec argon

<u>B</u> <u>(gauss)</u>	<u>Arc Voltage</u>	<u>Arc Current</u>
0	30	150
400	50	150
800	60	150
960	70	150
1120	80	150
1280	90	150
1600	100	150

At the high field strengths, arcing was observed from the cooling plates on the top and bottom of the magnet coils. No Hall deflection was observed in these experiments but a downward deflection on the cathode side of approximately 5 - 10 degrees was observed at fields of approximately 2000

gauss. Typical runs lasted for periods up to 10 minutes. Later inspection of the electrodes showed that the anode was in exceptionally good condition and that minor erosion had occurred along the upper portion of the cathode. Since the electrodes are operated in a horizontal position "upper" is used in a gravitational sense. The longitudinal thrust data for this run as interpreted from the output of the longitudinal transducer on the thrust stand are as follows:

70 grams - plasma jet only at 26 volts 300 amps 0.8 gm/sec argon
90 grams - arcs operating 30 volts, 150 amps
150 grams - arcs operating 50 volts, 150 amps, $B \sim 600$ gauss.

This corresponds to a specific impulse of 188 sec and an overall power efficiency of about 9%.

During all runs described above, the pole faces were covered with quartz plates. Otherwise the crossed field region was open.

With the plasma jet operating alone it was observed that the tail flame, which normally extends approximately 1 foot beyond the engine assembly (at a flow rate of 0.8 gm/sec and an operating power of 9 KW) was contracted toward the magnet assembly and that the jet took on a bushy appearance when magnetic field was increased to several kilogauss.

In view of the limited amount of thrust observed, a number of checks of the assembly were made to see if the low thrust readings were caused by interactions between the current in the plasma jet and arc leads and the magnetic field. With the magnetic field ranging from 0 - 10,000 gauss there was a negative thrust generated with the plasma jet and crossed field arcs inoperative. This negative deflection did not become serious until magnetic fields of the order of 3000 gauss were reached. Since the experiments used fields only up to 2000 gauss this effect was not believed to be influencing the thrust measurements. To seek current interaction effects, the anode and cathode were shorted by a bus bar and equivalent currents were passed through the system. No interaction was observed at zero magnetic field and as the field increased a slight negative interaction was observed. It was not serious at fields up to 2000 gauss.

In another series of thrust plate experiments a transite plate was mounted approximately 1 foot in front of the engine. This plate was swiveled at the lower edge and a thrust transducer was placed behind the plate. Although this system was not calibrated it gave a very sensitive indication of jet impingement. Thrust was observed with cold gas flows ranging from 0.5 - 2 gm/sec. With the plasma jet operating at approximately 9 KW

at 0.5 gm/sec of argon a hot spot was observed on the plate. This hot spot had a diameter of approximately 3/4 inch. . When the magnetic field was applied, the spot faded and at fields of the order of 1000 gauss there was no visual evidence of localized heating. The magnetic field had acted to disperse the jet over a wide area of the plate. The thrust level recorded with the plasma jet operating in zero magnetic field decreased with increasing field intensity. This indicated that the existing jet was being widely dispersed at the exit of the engine.

The table below shows the operating conditions for a typical 10 - 15 minute run, with cathode in No. 2 and No. 3 positions and the corresponding anodes in No. 1 and No. 2 position.

TABLE II

Chamber Pressure = 2.5 torr
Arc Current Maintained at 150 amps

Mass Flow Rate of Argon (gm/sec)	Plasma Jet Voltage (volts)	Current (amps)	Magnetic Field (gauss)	Arc Voltage (volts)
0.8	20	300	0	40
			320	50
			480	60
			640	70
			800	80
			1200	105
			1600	120
			0	30
0.6	26	300	320	50
			480	60
			640	75
			800	90
			1200	105
			1600	130
			0	30
			320	50

These tests have shown that arc operation can be obtained in a stable manner in magnetic fields of up to 2000 gauss for at least 15 minute periods. Staggering of the electrodes appeared to eliminate the Hall deflection of the beam but a definite downward deflection of the beam was observed. This downward deflection was probably caused by the fact that the plasma was not

symmetrical about the longitudinal axis of the accelerator and consequently deflection occurred in the fringing magnetic field.

B. LOW GAS FLOW EXPERIMENTS

1. Plasma Jet Performance

To operate the engine at argon flow rates below 0.5 gm/sec a special anode-nozzle, Figure 7, was designed. The copper nozzle had a throat diameter of 0.080 inch and diverged at a total angle of 26° to an exit diameter of 0.500 inch. The exit plane of the nozzle was 1.875 inches from the geometrical boundary of the poles of the magnet.

To measure thrust, the dynamometer was locked in a fixed position, and a thrust transducer was mounted behind a quartz deflection plate. The plasma jet beam was allowed to impinge upon this plate. The transducer was immersed in vacuum pump oil so as to cause it to be insensitive to changes in pressure in the test chamber.

Figure 26 shows the velocity of the jet as a function of the arc jet current at constant arc jet voltage for $\dot{m} = 0.25$ gm/sec argon. Also shown are the velocities for flow rates of 0.08, 0.13, 0.17, and 0.21 gm/sec at 300 amps. These velocities are obtained from

$$F_1 = \dot{m}v$$

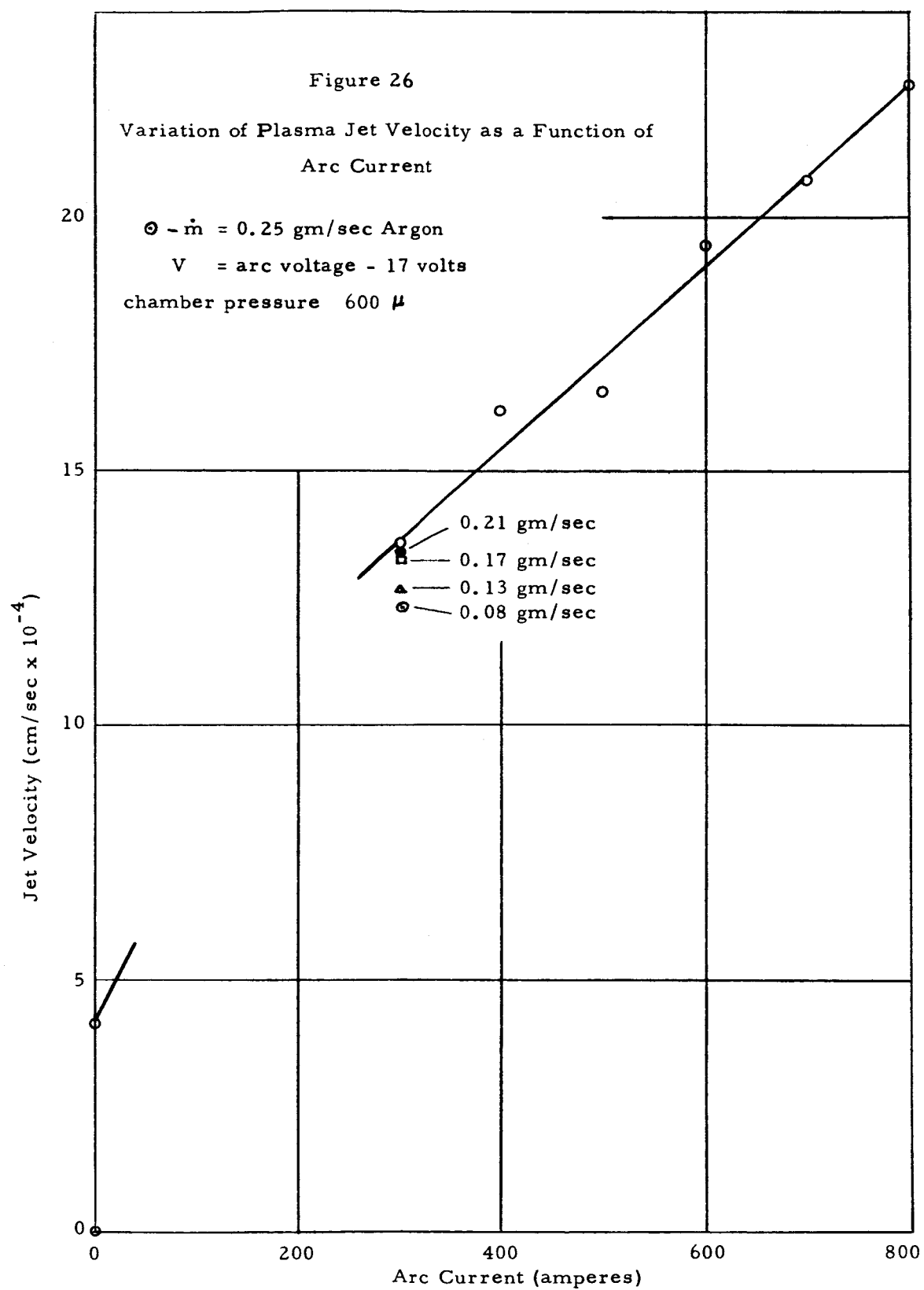
where F_1 is the measured thrust and \dot{m} the argon flow rate. This equation neglects the factor of

$$F_2 = A \Delta P$$

where ΔP is the difference in pressure between the end of the nozzle and the chamber, and A is the area of the exit of the nozzle. The chamber pressure varied from 600 μ with $\dot{m} = 0.3$ gm/sec to 250 μ with $\dot{m} = 0.1$ gm/sec. If the pressure at the exit of the nozzle were 1.5 mm Hg, the ratio $F_2/F_1 \approx 0.1$, i.e., a ten percent addition to the reactive term would be required.

2. Argon-Helium Mixtures

Stable operation with this anode-nozzle could be obtained with argon flow rates down to 0.04 gm/sec of argon at arc currents from 150 - 900 amperes at approximately 17 volts. Table III shows the variation



in arc voltage as a function of helium flow rate for a mixture of helium and argon. Over the range from approximately 0.05 gm/sec to 0.3 gm/sec of argon, the operating arc voltage of the mixture of He and A appears to depend only slightly on the helium flow rate. With an argon flow rate of 0.1 SCFM (0.08 gm/sec) there is only a 3 volt (or 19%) change in the arc voltage as the helium flow rate is increased from 0 to 75% of the total gas flow by volume (or from 0 to 24% of the total flow by mass).

TABLE III
Argon-Helium Mixtures
(Arc Current Constant at 100 Amperes)

Total SCFM	A SCFM	He SCFM	A gm/sec	H gm/sec	A % Volume	He % Volume	Arc Voltage volts	Chamber Pressure microns hg
0.1	0.1	0.0	0.08	0.0	100	0	16.0	350
0.2	0.1	0.1	0.08	0.008	50	50	17.5	600
0.3	0.1	0.2	0.08	0.016	33	67	18.0	900
0.4	0.1	0.3	0.08	0.024	25	75	19.0	1300
0.2	0.2	0.0	0.16	0.0	100	0	17.0	550
0.3	0.2	0.1	0.16	0.008	67	33	18.0	850
0.4	0.2	0.2	0.16	0.016	50	50	19.5	1250
0.5	0.2	0.3	0.16	0.024	40	60	20.0	1600
0.6	0.2	0.4	0.16	0.032	33	67	20.5	2000

3. Crossed Field Experiments

Figure 27 shows the arc voltage required to maintain a constant arc current in the crossed field region as a function of magnetic field strength. The relationship appears to be linear, at least up to 400 gauss, and is not as would be expected if the current density varied according to

$$j = \sigma_0 \sqrt{\frac{(E_y - U_z B)^2 + (E_z + U_y B)^2}{\Delta}}$$

as shown in Appendix I. The data was obtained using two pairs of electrodes staggered 1-1/2 inches on centers with the cathodes in positions number 2 and 3 and the corresponding anodes in positions number 1 and number 2. The electrode lateral separation was 1-1/4 inches and both anodes and cathodes were sheathed with boron nitride to within 3/4 inches of the tips. The data shown in Table IV is representative of the performance of the accelerator section using these two pairs of staggered electrodes. The thrust ratio refers

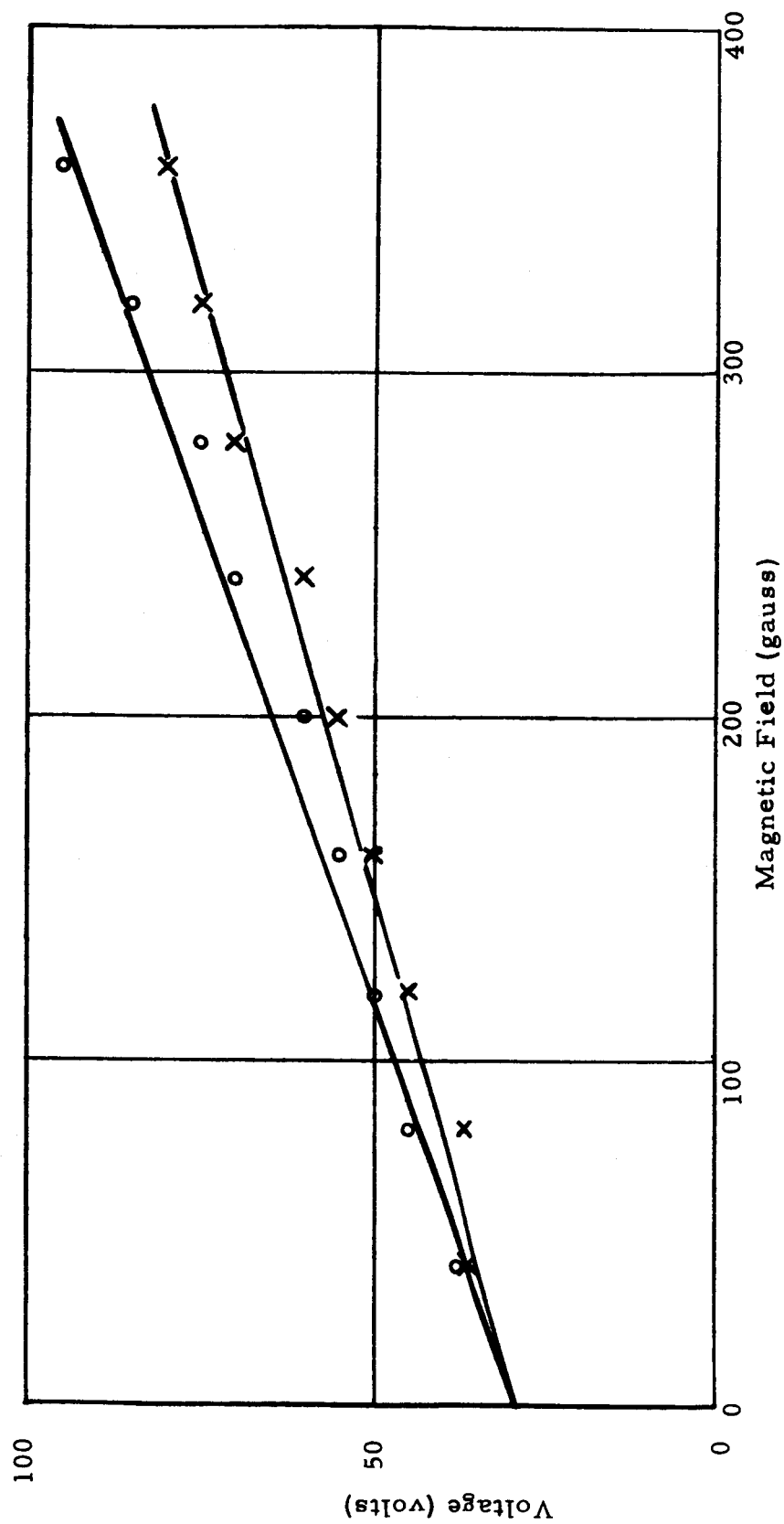


Figure 27

O - upstream electrodes maintained at 100 amps
 x - downstream electrodes maintained at 90 amps
 Plasma Jet Operated at 17.5 volts, 300 amps, 0.25 gms/sec Argon

Variation of Arc Voltage as a Function of Magnetic Field

to the thrust produced with the plasma jet and arcs operating at a certain magnetic field as compared to the thrust produced at zero magnetic field. Thrust was measured by allowing the beam to impinge upon a previously calibrated quartz deflection plate. Only ratios are shown since the exact fraction of the beam which struck the plate was not known. Figure 28 shows a recorder tracing of thrust data obtained in a typical run. The thrust decreased when the arcs were turned on, increased as the magnetic field was increased, and further increased when the magnetic field was decreased from 1143 gauss to zero.

The reason for this anomalous increase is not understood, but it is not due to magnetic effects in the thrust transducer itself. It is believed that the back EMF induced in the arc circuits due to the fairly rapidly decreasing magnetic field caused a large arc current surge, and consequently increased thrust. Full investigation of this effect has not been completed by the end of the present program. Figures 29a and 29b show the patterns obtained on the top and bottom quartz plates which protect the magnet pole faces, after about 30 minutes of operation. The anode insulators were severely eroded and anode arc attachment on the downstream anode, at least for one run, occurred on the copper portion of the electrode.

TABLE IV

PERFORMANCE OF ACCELERATOR USING TWO PAIRS OF STAGGERED ELECTRODES

Argon Flow Rate		0.25 grams/second	
Plasma Jet Voltage		18 volts	
Plasma Jet Current		300 amperes	
Plasma Jet Power		5.4 KW	
Upstream Electrode Current		100 amperes	
Downstream Electrode Current		90 amperes	
Magnetic Intensity B (gauss)	Thrust Ratio R	Total Arc Power, P_A (KW)	Total Power P_T (KW)
0	1.0	7.0	12.4
275	1.5	9.2	14.6
430	2.8	13.6	19.0
875	4.5	18.0	23.4
1143	6.0	22.0	27.4

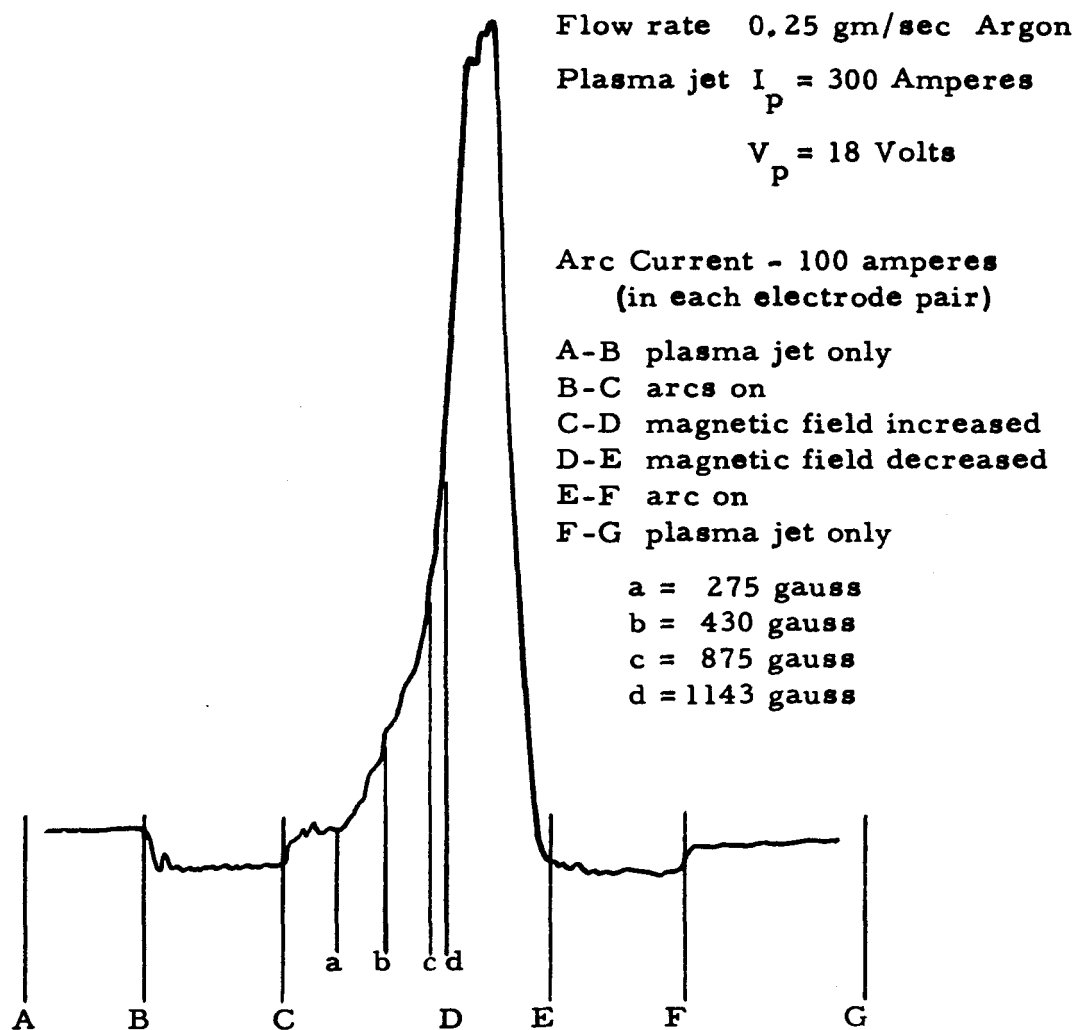


Figure 28. Recorder Tracing of Thrust Data



Figure 29.a. Photograph of Quartz Plate - Upper Plates

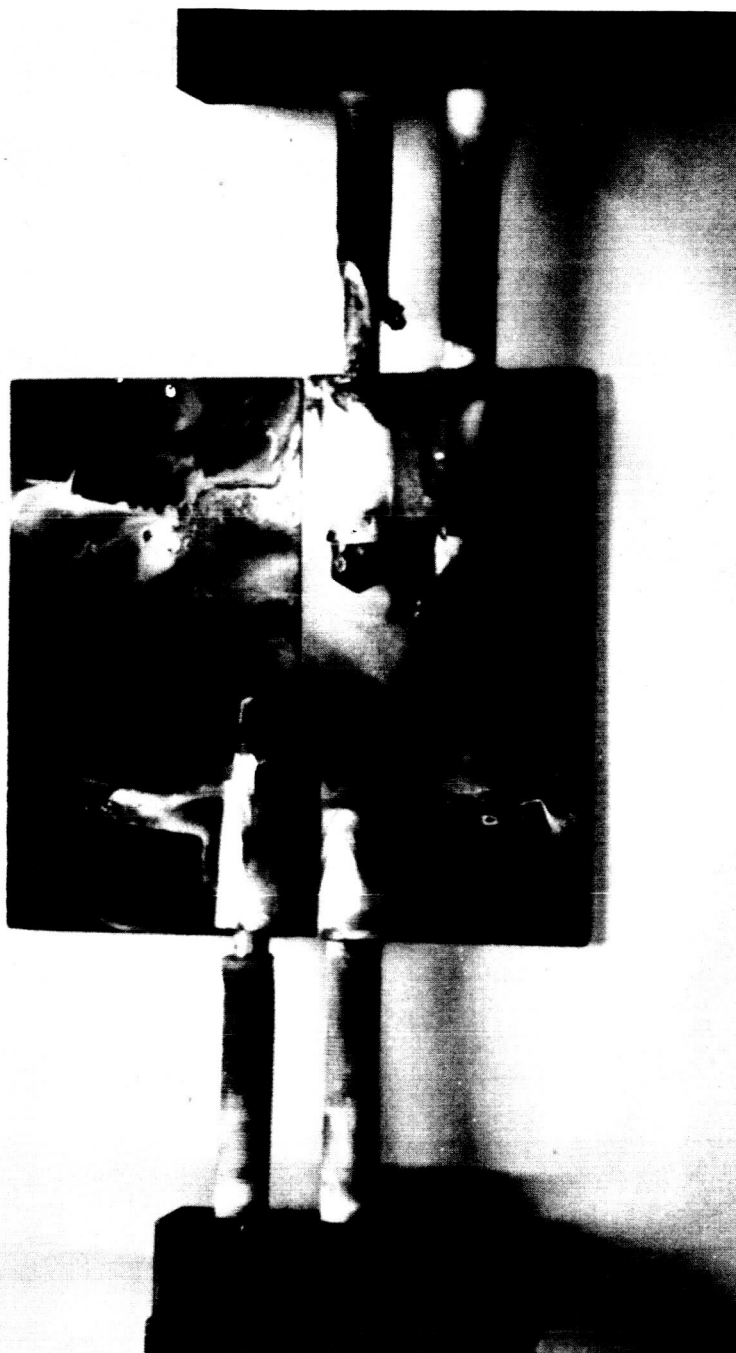


Figure 29.b. Photograph of Quartz Plate - Lower Plates

The electrode was covered with teflon but the teflon was quickly burnt away when arc attachment occurred. The copper patterns on the plates indicate that the arcs are driven a considerable distance downstream and that the jet was deflected slightly toward the cathodes.

The experiments described above have shown that electrode insulator erosion is extremely severe particularly when the electrodes are introduced perpendicular to the initial plasma flow direction. With zero external magnetic field there is a force due to the self-magnetic field of an electric arc which tends to expand the arc. The electrodes used had tungsten tips extending 1-1/4 inches back from the ends of the electrode. At high arc currents, the arc tended to attach at the anode on the copper portion above the tungsten tip because of the greater electrical conductivity of the copper. Since the water-cooling in this region was not particularly efficient, and vaporization of the copper occurred, the jet contained a high percentage of copper contamination.

The blowing effect of the partially ionized gas stream from the plasma jet, in combination with the magnetic force tended to force arc attachment to the downstream side of the anodes. When a magnetic field was applied, the arcs tended to expand toward regions of decreased field strength. In the case of the anodes, the attachment region was forced along the electrode on the downstream side and all insulators used were eroded well into the fringe region of the magnetic field.

As a result of these observations it appeared that the insulator erosion problem could be alleviated by introducing the electrodes parallel to the initial plasma stream direction, with the electrode tips lying just inside the fringing magnetic field. Figure 30 shows the arrangement of the electrodes used in an experiment to test this hypothesis. The magnetic field was directed into the plane of the diagram, and argon gas at 300° K, with no preionization, was introduced parallel to the electrodes through a 1/8 inch diameter stainless steel tube at a flow rate of approximately 0.2 gm/sec. The electrode tips were one inch out from the center line of the magnet.

With zero magnetic field, the arc ran at 45 volts with currents from 60 to 100 amperes. Runs were made with magnetic fields ranging up to 1000 gauss with the arc operating at this field value at 200 volts and 200 amperes. The runs lasted for periods of several minutes. Cathode attachment was good although there was some melting of the quartz insulator in the region around the point A, on the side of the electrode. Anode attachment occurred in the region around B where the tungsten tip joined the copper shaft, but did not proceed past this point. The transite plate on the bottom pole face of the magnet was partially eroded through in the region around C under the cathode,

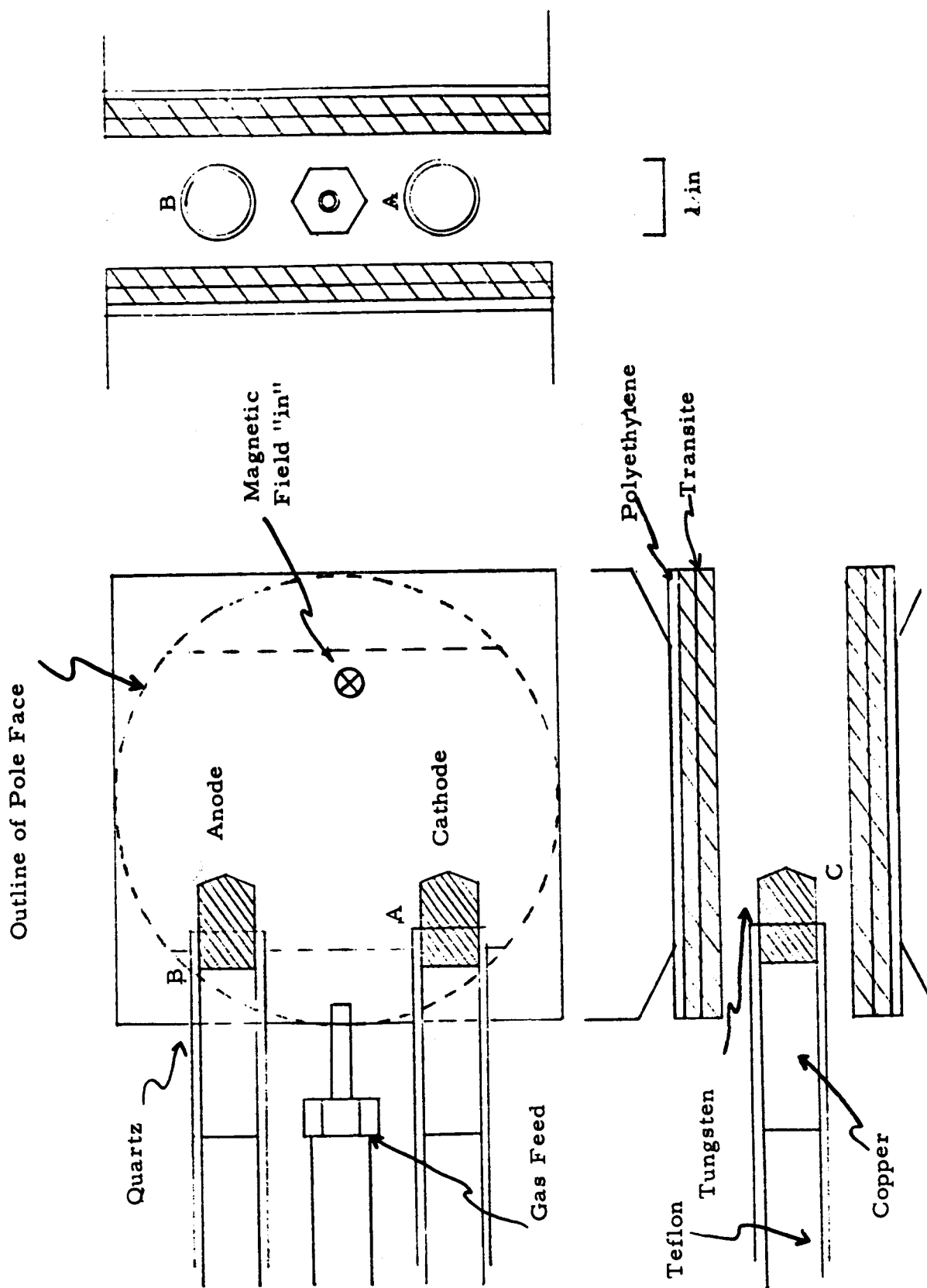


Figure 30. Electrode arrangement (with electrodes parallel to flow direction)

and there was some erosion on the bottom plate in front of the anode. The upper transite plate was not damaged although the polyethylene insulating plates showed signs of extreme heating. The arc pattern on the transite plates was unsymmetrical, being displaced toward the cathode side.

In another series of experiments a copper tipped anode, similar to that shown in Figure 5 was used. With an argon flow rate of approximately 0.1 gm/sec stable arc operation could be obtained for magnetic fields up to 2850 gauss. At this point the arc current was 240 amperes and the arc voltage was 200 volts. The anode showed some signs of surface melting after five minutes of operation but the cathode remained relatively unaffected except for the extreme tip region which showed that the tungsten had melted at this point. These results indicate the direction of further work in crossed field accelerator investigations.

IV

DIAGNOSTICS

Three techniques were used in an attempt to determine the electron density, electron temperature, and electron collision frequency in the plasma issuing from the arc jet. Langmuir probe measurements made at the center of the magnet gap with an argon flow rate of 0.2 gm/sec, and with the plasma jet operating at 300 amperes at 17 volts, gave an electron temperature T_e of approximately 5,000° K.

Attempts were made to compare this measurement with that obtained by optical methods utilizing a recording monochromometer. However, it was not possible to obtain a reproducible set of values for the intensities of the lines being observed. When helium was introduced into the argon flow, the helium lines were superimposed on a background of tungsten lines, thus making intensity measurements ambiguous. The tungsten lines only appeared when helium was present in the flow and it appears that the helium has an adverse effect upon the tungsten cathode of the plasma jet as far as sputtering of cathode material is concerned.

The most successful observations were made with the MHD Research, Inc. Model MDD-1-35PD microwave interferometer having an operating frequency of 35 Gc/s. The microwave horns were centered between the magnet gap at the number 2 electrode position with an effective interaction path length of 4 cm between the microwave signal and the plasma. The microwave interferometer provides a measurement of electron density by measurement of the phase change between two microwave paths. One path serves as a reference path and the other contains the plasma sample to be studied. If attenuation of the microwave signal across the sample path is kept small, the phase shift per unit length is directly proportional to the electron density. If attenuation of the signal is present, measurement of the phase shift and attenuation per unit length must be made unless estimates of the electron collision frequency are available. In the experiments that were conducted, the power levels were fixed and an arbitrary phase angle set before the plasma was allowed to stream across the sample path. The change in phase per unit path length through the sample and the attenuation per unit path may be expressed as

$$\frac{\Delta \phi}{Z} = \left(\frac{\omega_c n_e e^2}{2 c m \epsilon_0} \right) (\omega_c^2 + \omega^2)^{-1}$$

$$\frac{B}{Z} = \left(\frac{\omega_c n_e e^2}{2 c m \epsilon_0} \right) (\omega_c^2 + \omega^2)^{-1}$$

where

- $\Delta\phi$ - phase shift in radians
- Z - sample path length in meters
- ω - angular signal frequency
- B - signal attenuation in nepers
- n_e - electron density (meters)⁻³
- m - electron mass in kgm
- c - velocity of light in meters/sec
- ϵ_0 - dielectric constant of free space
- ω_c - angular collision frequency of the electrons
($= 2\pi\nu_c$)
- ν_c - electron collision frequency

With the plasma jet operating at 300 amperes at 17 volts with an argon flow rate of 0.2 grams per second, the phase shift was 200° and the attenuation 16 db or 1.84 nepers. Thus, for a 4 cm sample path,

$$n_e = 1.2 \times 10^{12} \text{ cm}^{-3}$$

$$\nu_e = 1.9 \times 10^{10} \text{ sec}^{-1}$$

the chamber pressure during these experiments was 600 microns Hg.

The electron temperature as obtained from the Langmuir probe measurements can be used in combination with the Saha equation to determine n_e , assuming singly ionized species only, since

$$\frac{n_e n_{A^+}}{n_A} = \frac{g_{A^+}}{g_A} \left(\frac{2\pi m k T_e}{h^2} \right)^{3/2} \exp. \frac{eV_A}{k T_e}$$

where

- n_{A^+} - concentration of singly ionized argon
- n_A - concentration of neutral argon
- g_A, g_{A^+} - ground-state degeneracies of the atoms and ions
- h - Planck's constant
- k - Boltzmann's constant
- V_A - first ionization potential of argon

For argon $g_A = 1$, $g_A^+ = 6$ and using $T_e = 5000^\circ\text{K}$ with the assumption the $n_e = n_A^+$,

$$\frac{n_e^2}{n_A} = 1.4 \times 10^6$$

By placing a tungsten wedge in the flow at the position at which the microwave measurements were made it was estimated that the gas temperature was approximately 3000°K , and that the Mach number of the flow was approximately 2.5 as determined from the angle of shock wave on the wedge. Thus, the neutral density n_A is estimated to be of the order of $2 \times 10^{17} \text{ cm}^{-3}$, which gives an electron density n_e of $5.3 \times 10^{11} \text{ cm}^{-3}$. This value of n_e is consistent with that obtained with the microwave data.

The conductivity of the plasma may be found by using σ_0 as given in Appendix I.

$$\sigma_0 = \frac{n_e e^2 t_e}{m_e} = \frac{n_e e^2}{m_e v_c}$$

where

$$t_e = \frac{1}{v_c}$$

Thus, with v_c as above, and $n_e = 1.2 \times 10^{12} \text{ cm}^{-3}$

$$\sigma_0 = 1.8 \text{ mho/m.}$$

This conductivity is very low and would not aid appreciably in arc-breakdown conditions. As far as the arcs are concerned, a cold gas stream could be used. This behavior has been verified experimentally by removing the plasma jet power while maintaining the same gas flow rate. Under these conditions the operating voltages and currents of the crossed field arcs remain essentially unchanged.

CONCLUSIONS

Under the present program a crossed field plasma accelerator system has been constructed, and data from approximately 20 hours of operation have been recorded. By using a specially designed low flow anode it has been possible to operate the plasma jet at argon flow rates as low as 0.04 gm/sec into a vacuum of less than 100 microns Hg, at power levels up to 20 KW. The efficiency of operation, however, is not known since the anode was not equipped to provide heat transfer data. Of all the system components, the plasma jet has caused the least difficulty and in the present state is capable of operating for many hours on a continuous basis.

With the zero magnetic field the accelerator section of the engine could also be operated for extended periods of time (greater than thirty minutes). On the other hand, the accelerator section, could only be operated continuously for periods of minutes at magnetic fields above 500 gauss, primarily because of severe erosion of insulating materials. The principal difficulty occurred from the tendency of the arcs to migrate along the electrode leads when the external magnetic field increased beyond several hundred gauss. Erosion of insulating plates on the top and bottom of the accelerator section was also severe, but in only one case was it necessary to terminate an experiment because of arcing to the magnet pole faces through these insulators. It is believed that material erosion could be significantly reduced by making three modifications to the present accelerator components. The first modification would involve increasing, by a factor of two, the distance between the electrode surfaces and the top and bottom insulating plates.

In the experiments described above, there was a tendency for arc attachment on the anodes to occur on the copper portion above the tungsten tips, probably because of the greater conductivity of copper. Therefore, a second change would be made by increasing the diameter of the anode to at least one inch and forming a hemispherical tip entirely of copper with adequate water cooling.

The cathode attachment in the experiments conducted was, in general, rather erratic. A much more stable mode of operation could be obtained if the cathode could be made to emit electrons thermionically from the whole cathode tip. Hence, the third modification would consist in increasing the cathode diameter to one inch and forming the tip from thoriated tungsten. The tip would be uncooled, and allowed to heat to the point of copious thermionic emission. This temperature could be controlled by adjusting the cathode cooling water supply.

The modifications suggested would mean increasing the magnet gap and this would result in a decrease in the maximum operating field. However, fields of several thousand gauss (e.g. ~ 2000 gauss) would still be available and such fields would be adequate for most experiments.

In early experiments with unstaggered electrodes a Hall deflection on the jet was observed. This deflection was largely eliminated by staggering the electrodes so that with a 1-1/4 inch spacing between electrode tips, the axis of cathodes were one and one-half inches upstream from the axis of the anodes. There still remained a jet deflection at the end of the accelerator, probably due to the interaction of the currents in plasma and the fringing field of the magnet. This deflection, in addition to the $\Phi \cdot (\vec{u} \times \vec{B}) \times \vec{B}$ interaction had the effect of spreading the beam and producing a net deflection in the downward direction.

Experiments with argon-helium mixtures have shown that it is possible to operate a constant current arc at a voltage which is very insensitive to the percentage of helium in the mixture, but depends mainly upon the argon flow rate. With an argon flow rate of 0.08 gm/sec there is only a 3 volt change in the arc voltage as the helium flow rate is increased from 0 to 75% of the total gas flow by volume or from 0 to 24% of the total flow by mass.

The Cardan hinge dynamometer, with the hinge thicknesses and alignments used, lacked the sensitivity to yield accurate thrust measurements at the thrust levels achieved with the accelerator at low gas flow rates. It is believed that the thrust in all low flow cases was less than 100 grams. However, the sensitivity of the system can be greatly improved by decreasing the hinge thicknesses and by careful alignment of the hinges. The quartz thrust plate was a very sensitive thrust indicator, but lacked accuracy.

The experiments which were performed with the arc electrodes introduced parallel to the initial flow direction and with the electrode tips in the fringing magnetic field indicate that insulator erosion can be considerably decreased and that stable arc operation can be obtained in high magnetic fields at high power levels.

VI. REFERENCES

1. Demetriades, S. T., et al, Preprint No. 2375-62, ARS Electric Propulsion Conference, March 1962.
2. Russel, G. R., Byron, S., Bortz, P. I., Preprint No. 63-005, AIAA Electric Propulsion Conference, March 1963.
3. Sherman, A., J.A.R.S., 3, 414 (1962).
4. Sutton, G. W., J. Appl. Phys., 34, 396 (1963).
5. Sutton, G. W., Hurwitz, H., Kibb, R. W., J. Appl. Phys., 32, 205 (1961).
6. Denison, M. R. and Ziemer, R. W., Preprint No. 63-378, AIAA 5th Biennial Gas Dynamic Symposium, August 1963.
7. Oates G. C., AIAA Journal 1, 2785 (1963).

APPENDIX I

Accelerator Theory

A. LIST OF SYMBOLS

ρ	plasma density
\vec{u}	plasma velocity
p	plasma pressure
T	plasma temperature
\vec{B}	magnetic induction in stationary reference frame
\vec{E}	electric field intensity in stationary reference frame
\vec{E}'	electric field intensity in reference frame moving with velocity \vec{u} , $(\vec{E}' = \vec{E} + \vec{u} \times \vec{B})$
\vec{j}	current density
m_i	ion mass
e	electron charge
$(\tau_{ia})^{-1}$	ion-atom collision frequency
$(\tau_e)^{-1}$	$(\tau_{ea})^{-1} + (\tau_{ei})^{-1}$
$(\tau_{ea})^{-1}$	electron-atom collision frequency
$(\tau_{ei})^{-1}$	electron-ion collision frequency
m_e	electron mass
τ	viscous stress tensor
e_g	total energy of the plasma per unit mass, $e_g = U_g + \frac{u^2}{2}$

U_g total internal energy of the plasma per unit mass

h enthalpy of the plasma, $h = U_g + \frac{p}{\rho} = C_p T$

k coefficient of heat conductivity (in general a function of T)

C_p specific heat at constant pressure

μ_0 magnetic permeability

Φ conductivity tensor

For a weakly ionized gas in which the gradient of the electron pressure is negligible, the conductivity tensor Φ is a function of the components of \vec{B} , the zero \vec{B} field conductivity σ_0 , the Hall parameter γ , and the ion slip parameter γ_2 , where Φ , σ_0 , γ_1 and γ_2 are given by

$$\Phi^{-1} = \frac{1}{\sigma_0} \left[I + \sigma_0 \gamma_1 (I \times \vec{B}) - \sigma_0 \gamma_2 (I \times \vec{B})^2 \right]$$

where I is the unit dyadic.

$$\sigma_0 = \frac{n_e e^2}{m_e}$$

$$\gamma_1 = \frac{1}{n_e} \quad \text{Hall parameter}$$

$$\gamma_2 = \frac{\gamma_1 f^2 \theta_{ia}}{B} \quad \text{ion slip parameter}$$

where

n_e = electron concentration

$$f = \frac{n_a}{n_e + n_a}$$

n_a — neutral atom concentration

$$\theta_{ia} = 2\omega_i \tau_{ia}$$

$$\omega_i = \frac{eB}{m_i}$$

B. FUNDAMENTAL EQUATIONS

The fundamental equations governing the steady state behavior of a crossed field plasma accelerator are listed below, assuming the plasma is electrically neutral and behaves as a perfect gas.

$$\begin{aligned}
 \nabla \cdot \rho \vec{u} &= 0 && \text{Continuity} \\
 p &= \rho RT && \text{State} \\
 \rho \vec{u} \cdot \nabla \vec{u} &= - \nabla p + \nabla \cdot \tau + \vec{j} \times \vec{B} && \text{Motion} \\
 \nabla \cdot \rho e \vec{u} &= - \nabla \cdot p \vec{u} + \nabla \cdot (\vec{u} \cdot \tau) + \nabla \cdot (k \nabla T) + \vec{j} \times \vec{E}' && \text{Energy} \\
 \text{or} \\
 \rho \vec{u} \cdot \nabla (h + \frac{u^2}{2}) &= \nabla \cdot (\vec{u} \cdot \tau) + \nabla \cdot (k \nabla T) + \vec{j} \times \vec{E}' \\
 \vec{j} &= \Phi \cdot \vec{E}' && \text{Ohms Law} \\
 \nabla \times \vec{B} &= \mu_0 \vec{j} && \text{Maxwells' Equations} \\
 \nabla \times \vec{E} &= 0 \\
 \nabla \cdot \vec{B} &= 0
 \end{aligned}$$

C. CURRENT DENSITY COMPONENTS

The tensor conductivity, in the case of a weakly ionized gas (f x l) is given by the increase of the tensor

$$\Phi^{-1} = \frac{1}{\sigma_0} \left[I + \sigma_0 \gamma_1 \cdot (I \times \vec{B}) - \sigma_0 \gamma_2 \cdot (I \times \vec{B})^2 \right]$$

where I is the unit dyadic.

If \vec{B} is directed along the negative x - axis (Figure 1) and \vec{E} has components E_y and E_{z_1} then

$$\Phi = \frac{\sigma_0}{\Delta} \begin{bmatrix} 1 & 0 & 0 \\ 0 & (1 + \theta_e \theta_{ia}) & \theta_e \\ 0 & -\theta_e & (1 + \theta_e \theta_{ia}) \end{bmatrix}$$

where

$$\Delta = (1 + \theta_e \theta_{ia})^2 + \theta_e^2$$

$$\theta_e = \omega_e \tau_e$$

$$\omega_e = \frac{eB}{m_e}$$

The current density may be written as

$$\vec{j} = \Phi \cdot \vec{E}' = \sigma_0 \left[\vec{E}' - \gamma_1 (\vec{j} \times \vec{B}) + \gamma_2 (\vec{j} \times \vec{B}) \times \vec{B} \right]$$

The components of the current density are:

$$j_x = 0$$

$$j_y = \frac{\sigma_0}{\Delta} \left[(E_y - U_z B) (1 + \theta_e \theta_{ia}) + (E_z + U_y B) \theta_e \right]$$

$$j_z = \frac{\sigma_0}{\Delta} \left[(E_z + U_y B) (1 + \theta_e \theta_{ia}) - (E_y - U_z B) \theta_e \right]$$

The total current density is

$$j = \sqrt{j_y^2 + j_z^2}$$

$$= \sigma_0 \sqrt{\frac{(E_y - U_z B)^2 + (E_z + U_y B)^2}{\Delta}}$$

D. VELOCITY INTERACTION

Ohm's Law, in the absence of an applied electric field becomes

$$\vec{j} = \Phi \cdot (\vec{u} \times \vec{B})$$

Hence, the equation of motion (neglecting pressure and viscous terms) becomes

$$\rho \vec{u} \cdot \nabla \vec{u} = \left[\Phi \cdot (\vec{u} \times \vec{B}) \right] \times \vec{B}$$

Thus, there will be an interaction between the conducting plasma and the magnetic field even with externally applied electric field.

APPENDIX II

Thrust Measurement with Thin Flexure Dynamometry

Two common methods of direct thrust measurement include: (1) causing the jet beam to impinge upon some target which senses and measures the thrust, or (2) floating or suspending the engine and measuring the reactive force exerted upon it. The latter method will be considered in this discussion. Manifold difficulties and uncertainties are encountered in thrust target measurements including: uncertainty of efficiency of momentum transfer (collecting beam and causing a 90° deflection), disruption of flow, burning or melting away of the target and, inherent with a $\vec{J} \times \vec{B}$ device, the necessity of applying a constantly varying and poorly defined angle of incidence correction caused by the Hall current beam deflection. It then becomes apparent that, for any reasonable degree of thrust measurement accuracy, some type of reactive force measurement must be adopted.

A few reactive force devices currently in use include; the thrust cart (engine is mounted on a wheeled vehicle), the ballistic pendulum, critically loaded columns, and thin flexures of the Cardan hinge type operating in one degree of freedom. Each has obvious advantages but all have disadvantages for application to a $\vec{J} \times \vec{B}$ thrust dynamometer. Notable disadvantages are excessive friction, single degree of freedom or inability to prevent rotational forces which cause crossfeed and confusion of supposedly independent data.

Since a two-component thrust will be experienced with a $\vec{J} \times \vec{B}$ engine, two independent suspensions are required to obtain measurements of both components. Thus, a special dynamometer has been developed.

The working members in this dynamometer are thin flexures called Cardan hinges. Figure 31 illustrates the construction of a Cardan hinge flexure.

The thin flexures in the Cardan hinge allow for ease of movement resulting from forces parallel to A-A but are extremely rigid to forces parallel to B-B. By properly matching the flexure thickness to the load it is possible to design for positive or zero restoring force in which case the hinge acts as a nearly frictionless bearing, frictionless except for molecular friction.

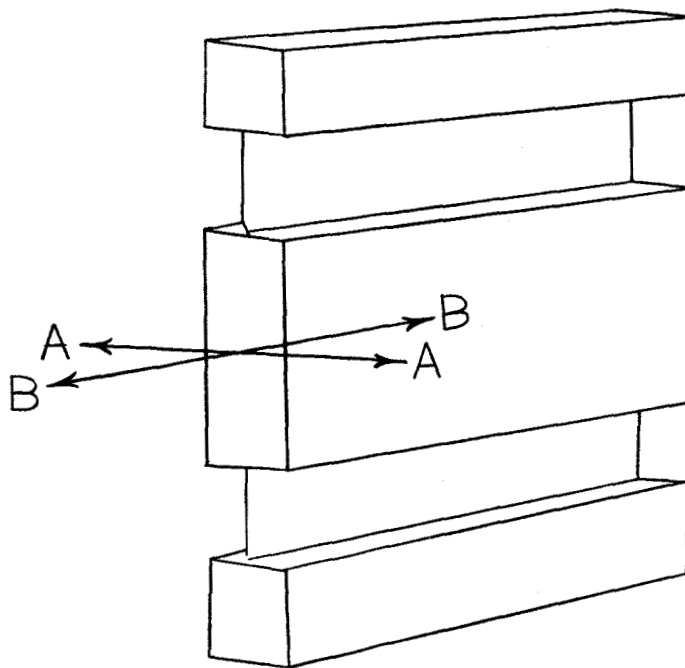
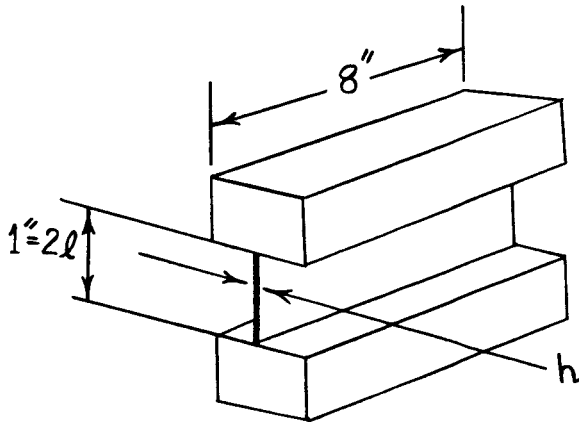


Figure 31. Cardan Hinge

Using two pairs of Cardan hinges, orthogonally, it is possible to have non-rotating free motion in a plane, an advantage not afforded by either a ballistic pendulum or critically loaded columns.

a. Stability Calculations

Determination of hinge thickness (h) with reference to the sketch below, the load per flexure plate is



$$p = \frac{1}{2} \times 800 = 400 \text{ lbs}$$

Allowing a factor of four on the Euler critical load

$$W = 4 \times 400 = 1600 \text{ lbs.}$$

i.e., the hinge is to be designed to support four times the buckling load

$$b = \text{width} = 8 \text{ inches}$$

The free-free column length ℓ (for a column with both ends movable) is:

$$\ell = \frac{1}{2} \times 1 = 1/2 \text{ inch.}$$

The critical load for such a column is given by

$$W = \frac{\pi^2 EI}{\ell^2 (1 - \mu^2)}$$

where E is the Young's modulus, I the geometrical moment of inertia, and μ is Poisson's ratio.

For a long, thin stainless steel column

$$I = \frac{bh^3}{12}$$

$$E = 2.8 \times 10^7 \text{ psi}$$

$$\mu \approx 0.3$$

so

$$W = \frac{\pi^2 E b h^3}{12 \times 0.91 \ell^2}$$

$$h^3 = \frac{12 \times 0.91 \times 1.6 \times 10^3 \times (5 \times 10^{-1})^2}{\pi^2 \times 2.8 \times 10^7 \times 8}$$

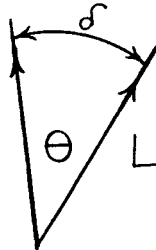
$$h = 1.26 \times 10^{-2} \text{ in.}$$

The direct axial stress is

$$S = \frac{P}{A} = \frac{W}{4bh} = 4000 \text{ lbs in}^{-2}$$

b. Pendulum-Type Forces

The system as constructed behaves as an inverted pendulum. Consider a small displacement δ .



The force tending to upset the system is

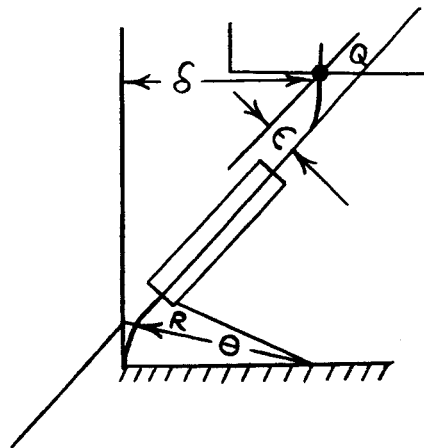
$$C_1 = \frac{P \delta}{L}$$

The load C_2 along the hinge is

$C_2 = P \cos \theta \approx P$. Since the maximum allowable displacement is $\delta = 0.0015$ inch, as determined by the strain gage, and the vertical length of the hinge is $L = 8$ inches, the upsetting force is

$$C_1 = 0.075 \text{ lbs.}$$

c. Bending Load Associated with Eccentric Application of the Load in a Deflected Position



If the load is displaced a distance δ , the radius of curvature of the flexure is

$$R \approx \frac{\ell}{\theta}$$

also

$$\theta \approx \frac{\delta}{L}$$

so

$$R \approx \frac{\ell L}{\delta}$$

Using the maximum allowable deflection

$$\delta = 0.0015 \text{ inch}$$

$$R \approx \frac{1 \times 8}{1.5 \times 10^{-3}} \approx 5.33 \times 10^3$$

The displacement ϵ is given by

$$\epsilon = R (\sec \theta - 1) \frac{R \theta^2}{2}$$

$$\approx \frac{\ell L}{\delta} \frac{\delta^2}{2L^2} \frac{\ell \delta}{2L}$$

and the moment about point Q is

$$M_1 = C_2 \epsilon = 400 \times \frac{1 \times 1.5 \times 10^{-3}}{2 \times 8}$$

$$= 3.75 \times 10^{-2} \text{ in.-lbs}$$

The maximum fiber stress T_m is

$$T_m = \frac{M_1 y_n}{I} = \frac{M_1 h}{2 I}$$

$$= \frac{3.75 \times 10^2 \times 1.26 \times 10^{-2}}{2 \times \left[\frac{8 \times (1.26 \times 10^{-2})^3}{12} \right]}$$

$$= 1.77 \times 10^2 \text{ psi}$$

on the order of 4% of direct axial stress.

d. Neutral Stability

Flexure plates can be designed for approximate neutral pendulum stability of the entire assembly. To achieve this, the moment $\frac{W\delta}{2}$ should be equal to that required to bend the plate through angle θ or to radius R.

Thus:

$$(1 - \mu^2) \frac{M_2}{EI} = \frac{d^2 y}{dx^2} = \frac{1}{R} \quad (x \text{ and } y \text{ are beam coordinates})$$

$$(1 - \mu^2) \frac{P\delta}{EI} = \frac{1}{R} = \frac{1}{L/\theta} = \frac{\theta}{L} = \frac{\delta}{L\ell}$$

$$I = (1 - \mu^2) \frac{PL\ell}{E} \text{ per flexure plate}$$

$$I = \frac{bh^3}{12} = 1.04 \times 10^{-4}$$

then

$$h = 0.0538 \text{ inches}$$

At this flexure thickness, the elastic restoring force would approximately balance the inverted pendulum effect to prevent toppling. If h^3 were doubled, the dynamometer would return to the neutral center, as if suspended as a conventional pendulum (provided it were initially leveled).

With the thickness of the flexures now determined the next step is to provide for mounting two pairs of Cardan hinges, orthogonally, in some manner other than stacking them one upon the other. This was accomplished by mounting one set between the engine and a movable platform, and the other set between this movable platform and the base plate. A drawing (minus bracing and gusseting) is enclosed as Figure 14.

To measure the transverse component of thrust (due to Hall current deflection of the beam) another departure from the normal orientation of the engine was made. Most engines of the $\vec{J} \times \vec{B}$ type are run with the "E" field electrodes oriented in a vertical mode. The problem then would be to measure a fraction of a pound in 800 pounds (engine weight). It is difficult to accomplish this with the required degree of accuracy since the weight of the engine obscures the transverse thrust. To avoid this problem, and to yield sensitive measurements, the "E" field electrodes are oriented in the horizontal mode. This yields an unencumbered horizontal thrust component. Both longitudinal and transverse thrust components are then horizontal.

To prevent extraneous forces or restraints from being imposed upon the dynamometer, all electrical connections are made through mercury pots. A probe from each electrical fitting is immersed in a pool of mercury which completes the circuit and simultaneously provides a completely flexible connection. The cooling water connections are not as readily handled but an effort has been made to dynamically balance all water forces and to reduce force couples to a minimum.

APPENDIX III

ANALYTICAL STUDIES OF ($\vec{J} \times \vec{B}$) ACCELERATOR

The analytical program to be carried out by the Marquardt Corporation was deleted from the work statement during the third quarter of the contract in order to supply a larger effort on the more important experimental program. Although definite results are not obtained, the progress made up to the deletion of the analytical portion is described below. A major portion of the time was spent on analyzing heat transfer and friction effects applicable to the desired range of mass flow and specific impulse in the presence of crossed electric and magnetic fields. The kinetic theory analysis, as well as Hall effect studies, were started but, because of lack of time and insufficient experimental data, did not advance to a point where any significant results can be reported.

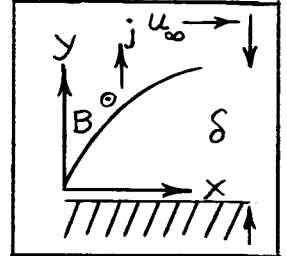
A. Heat Transfer and Friction Effects

Of all the criteria affecting the performance of electrical propulsion systems for space missions, the requirements of high power conversion efficiency and long engine life are probably most important. This is particularly true of crossed field ($\vec{J} \times \vec{B}$) accelerators, where the electrodes must maintain structural integrity with minimal heat loss in the presence of a high velocity plasma stream and a high current density gaseous discharge. Therefore, a study of the flow phenomena over the $\vec{J} \times \vec{B}$ accelerator electrodes is necessary to obtain a better knowledge of the parameters affecting electrode heat transfer and heat transfer rates.

Previous investigations (Ref. 1 & 2) of heat transfer and friction effects in magnetogasdynamic channel flow have utilized the conventional boundary layer equations modified by the addition of an electromagnetic body force term in the momentum equation, and a joule dissipation term and an electron enthalpy transport term in the energy equation. However, use of the boundary layer equations implies that an order of magnitude analysis has been made to obtain the simplified forms of the momentum and energy equations. Thus, there must be some bounds on the electromagnetic terms appearing in these two equations. These bounds must be defined before any type of boundary layer analysis can be employed. The following flow model was assumed to determine what bounds must be placed on the electromagnetic terms:

- a) steady, compressible, two dimensional flow
- b) the current density is a constant perpendicular to the electrode surface, and is determined by conditions in the free stream

- c) the magnetic flux density is perpendicular to both the current density and the free stream velocity
- d) the boundary layer thickness (δ) is much less than some characteristic accelerator dimension (ℓ)



It is also assumed that the fluid electrical conductivity is a scalar, the specific heat, c_p , is a constant, and that the electron temperature can be different from the ion and neutral temperature. Finally, it is assumed that the magnetic Reynolds number ($R_m = \sigma_\infty \mu_\infty u_\infty \ell$) is less than unity. This assumption infers that the magnetic field is essentially unaffected by the gas motion (the magnetic field induced by currents in the flow is small relative to the applied field), thereby uncoupling Maxwell's equations from the fluid dynamic equations. With these assumptions, the equations governing the flow are given by:

continuity:

$$\frac{\partial}{\partial x} (\rho u) + \frac{\partial}{\partial y} (\rho v) = 0 \quad (1)$$

x-momentum:

$$\rho u \frac{\partial u}{\partial x} + \rho v \frac{\partial u}{\partial y} = jB - \frac{\partial p}{\partial x} + \frac{\partial}{\partial x} \left[\mu \left(\frac{2\partial u}{\partial x} - \frac{2}{3} \left(\frac{\partial u}{\partial x} + \frac{\partial v}{\partial y} \right) \right) \right] + \frac{\partial}{\partial y} \left[\mu \left(\frac{\partial u}{\partial y} + \frac{\partial v}{\partial x} \right) \right] \quad (2)$$

y-momentum:

$$\rho u \frac{\partial v}{\partial x} + \rho v \frac{\partial v}{\partial y} = -\frac{\partial p}{\partial y} + \frac{\partial}{\partial y} \left[\mu \left(\frac{2\partial v}{\partial y} - \frac{2}{3} \left(\frac{\partial u}{\partial x} + \frac{\partial v}{\partial y} \right) \right) \right] + \frac{\partial}{\partial x} \left[\mu \left(\frac{\partial u}{\partial y} + \frac{\partial v}{\partial x} \right) \right] \quad (3)$$

energy:

$$\begin{aligned} \rho u c_p \frac{\partial T}{\partial x} + \rho v c_p \frac{\partial T}{\partial y} = & u \frac{\partial p}{\partial x} + v \frac{\partial p}{\partial y} + \frac{\partial}{\partial x} \left(k \frac{\partial T}{\partial x} \right) + \frac{\partial}{\partial y} \left(k \frac{\partial T}{\partial y} \right) \\ & + 2\mu \left[\left(\frac{\partial u}{\partial x} \right)^2 + \left(\frac{\partial v}{\partial y} \right)^2 \right] + \mu \left(\frac{\partial v}{\partial x} + \frac{\partial u}{\partial y} \right)^2 - \frac{2}{3} \mu \left(\frac{\partial u}{\partial x} + \frac{\partial v}{\partial y} \right)^2 \\ & + \frac{j^2}{\sigma} + \frac{5}{2} \frac{k}{e} \left[\frac{\partial}{\partial x} (j T_e) + \frac{\partial}{\partial y} (j T_e) \right] \end{aligned} \quad (4)$$

non-dimensionalizing in the following manner

$$\rho^* = \rho / \rho_\infty$$

$$u^* = u / u_\infty$$

$$T^* = T / T_\infty$$

$$Re_\infty = \rho_\infty u_\infty l_\infty / \mu_\infty$$

$$Pr_\infty = \mu_\infty C_p / K_\infty$$

$$\rho^* = \rho / \rho_\infty$$

$$v^* = v / v_\infty$$

$$Te^* = Te / Te_\infty$$

$$M_\infty^2 = \rho_\infty u_\infty^2 / \gamma \rho_\infty$$

$$\mu^* = \mu / \mu_\infty$$

$$K^* = K / K_\infty$$

$$x^* = x / l$$

$$y^* = y / \delta$$

the continuity equation yields the result that

$$\frac{v_\infty}{u_\infty} = 0 \left(\frac{\delta}{l} \right) \quad (5)$$

the momentum equation in the x-direction gives

$$Re_\infty = 0 \left(\frac{l^2}{\delta^2} \right) \quad (6)$$

$$jBl = 0(\rho_\infty u_\infty^2) \quad (7)$$

while the momentum equation in the y-direction gives

$$\frac{\partial \rho^*}{\partial y^*} = 0 \left(\frac{\delta^2}{l^2} \right) \quad (8)$$

That is, the pressure is a function of x only, and is constant across the boundary layer. The energy equation yields the result that

$$Pr_\infty = 0(1.0) \quad (9)$$

$$\frac{5}{2} j k T e_\infty = 0 \left[\frac{\delta}{l} e \rho_\infty u_\infty C_p T_\infty \right] \quad (10)$$

$$\frac{j^2 l}{\sigma_\infty} = 0(\rho_\infty u_\infty C_p T_\infty) \quad (11)$$

Equations (7) and (11) can be combined to eliminate j, and together with the equation of state, give

$$\frac{\sigma_{\infty} B^2 l}{\rho_{\infty} u_{\infty}} = \frac{Ha_{\infty}^2}{Re_{\infty}} = 0 \left(\frac{u_{\infty}^2}{C_p T_{\infty}} \right) = 0 \left((\gamma - 1) M_{\infty}^2 \right) \quad (12)$$

For low supersonic Mach numbers equation (12) states that the ratio of the electromagnetic force to the inertia force must be of the order of unity. For Reynolds numbers much greater than unity, it is also seen that the Hartmann number (Ha-ratio of electromagnetic to viscous forces) must be greater than unity. Combining equation (12) with the assumption of small magnetic Reynolds number gives after some manipulation

$$\frac{B^2}{\mu_0} = 0 \left[\gamma (\gamma - 1) \frac{M_{\infty}^4 \rho_{\infty}}{R_m} \right] \quad (13)$$

Equation (11) can be put into the form

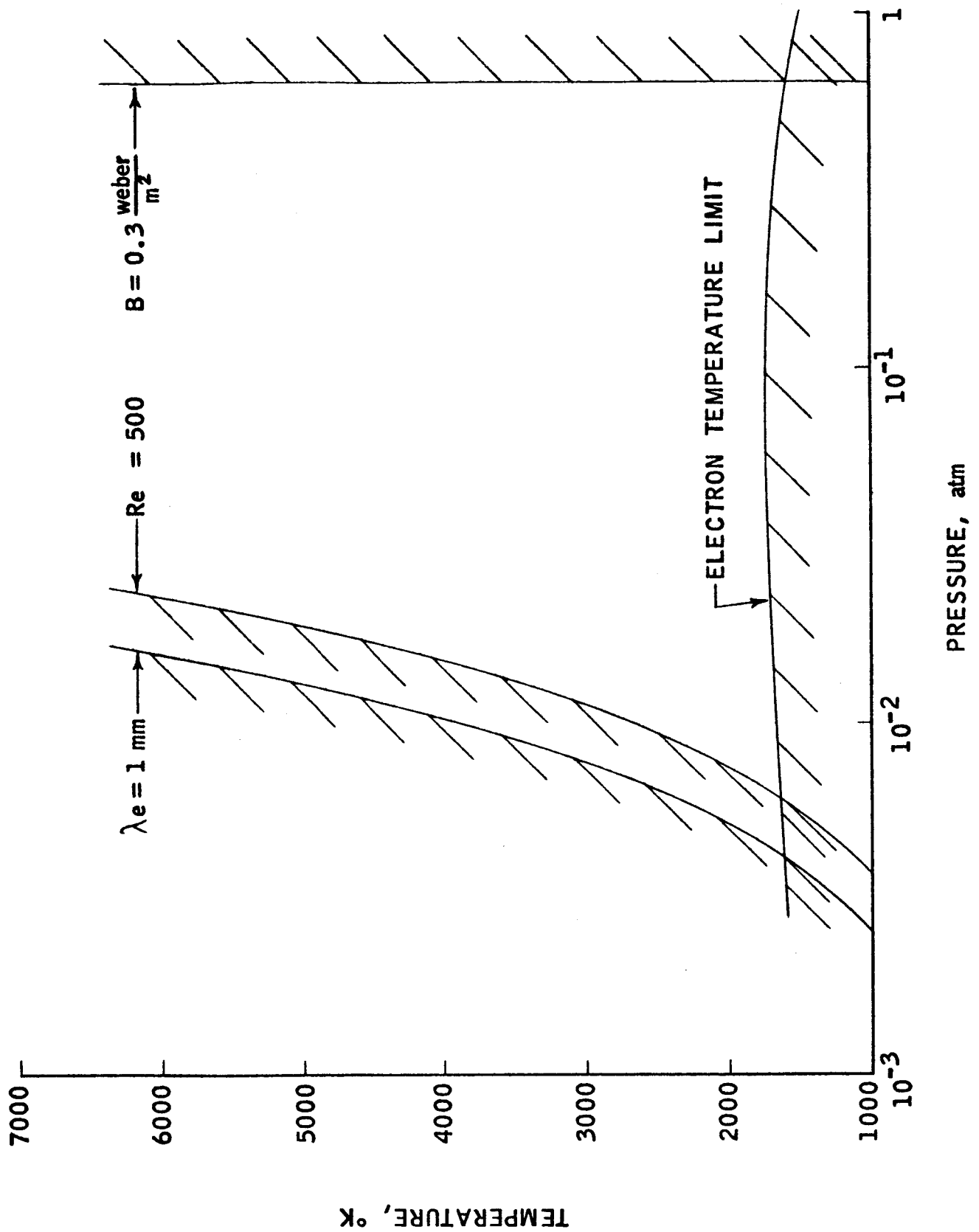
$$j^2 = 0 \left[R_m \left(\frac{\gamma}{\gamma - 1} \right) \frac{\rho_{\infty}}{\mu_0 l^2} \right] \quad (14)$$

With the aid of the preceding equations, the regions of validity of the boundary layer analysis can now be discussed. The flow must be a continuum for the concept of a boundary layer to be a reality. This implies that the mean free path of an electron must be much smaller than the boundary layer thickness. Figure 32 shows the required temperatures and pressures to obtain an electron mean free path of 1.0 mm in helium (The characteristic length is assumed to be 0.1 m, and the collision cross-section was obtained from Reference 3).

An even more stringent requirement in terms of accelerator static pressure is that the boundary layer thickness must be much smaller than the characteristic length. From equation (6), it is seen that this requirement is satisfied for Reynolds numbers greater than approximately 400. A line for $Re = 500$ is plotted on Figure 32, assuming a Mach number of unity. Note that $p_{\infty} = 10^{-2}$ atm, $T_{\infty} = 3000$ K, which is roughly the operating point of the accelerator work done under Contract NAS 5-1120, falls nearly on the $Re_{\infty} = 500$ line.

It was shown previously (e.g. (11) - (13)) that for a given magnetic flux density, the pressure had to be below some maximum value to insure that the inertia force be of the order of the electromagnetic body force. The maximum accelerator static pressure for $B = 0.3$ weber / m² (3000 gauss) is shown in Figure 32 to be 0.64 atm.

REGIONS OF VALIDITY OF THE BOUNDARY LAYER ANALYSIS



R-14,743

Figure 32

The order of magnitude of the current density applicable to this analysis is given by equation (14). This equation can be combined with equations from Reference (4) relating current density to electron temperature, degree of ionization, and electrical conductivity. Eliminating the current density from equations (10) and (11), and using the calculated electrical conductivity, an estimate of the electron temperature applicable to this analysis can be obtained. This was done for helium propellant seeded with 1.0 percent cesium. The resultant limit line shown in Figure 32 gives minimum ion-neutral temperatures of about 1600K and is nearly independent of accelerator static pressure. At ion-neutral temperatures below this value, the electron temperature rises to values sufficiently high to invalidate the order of magnitude argument presented previously.

One final limit line that might be plotted on Figure 32 is the line for a magnetic Reynolds number of unity. However, with a Mach number of unity and a characteristic length of 0.1 meter, the electrical conductivity must be greater than 10^3 mho/meter. Electrical conductivities of this magnitude cannot be obtained with a 1 percent cesium seeding and with the current density specified by equation (14). However, for higher seed ratios and greater current densities, there will be some upper limit to the accelerator static temperature.

Therefore, it can be concluded from the results given in Figure 32 that the boundary layer equations supplemented by the electro-magnetic terms can be employed for accelerator static pressures between approximately 10^{-2} atm. and 1 atm., and for accelerator static temperatures greater than roughly 1600K. The operating regime of the $\vec{J} \times \vec{B}$ accelerator is expected to fall within these bounds.

The appropriate boundary layer equations obtained from the order of magnitude simplification of equations (1) through (4) then become

$$\frac{\partial}{\partial x}(\rho u) + \frac{\partial}{\partial y}(\rho v) = 0 \quad (1)$$

$$\rho u \frac{\partial u}{\partial x} + \rho v \frac{\partial u}{\partial y} = jB - \frac{d\rho}{dx} + \frac{\gamma}{\partial y} \left(\mu \frac{\partial u}{\partial y} \right) \quad (15)$$

$$\rho u C_p \frac{\partial T}{\partial x} + \rho v C_p \frac{\partial T}{\partial y} = u \frac{d\rho}{dx} + \mu \left(\frac{\partial u}{\partial y} \right)^2 + \frac{j^2}{\sigma} \quad (16)$$

$$+ \frac{\partial}{\partial y} \left(k \frac{\partial T}{\partial y} + \frac{5}{2} j \frac{k}{e} T_e \right)$$

These equations, together with the equation of state, must be supplemented by equations relating electron temperature and ion-neutral temperature and ion-neutral temperature to electrical conductivity. From Reference (4), the electron temperature as a function of the other variables is

$$\frac{T_e}{T} = 1 + \frac{m_a}{\alpha^{3/4} k T} \left(\frac{j}{e n_e} \right)^2 \quad (17)$$

With the assumption that ionization equilibrium is attained at the electron temperature, the electron concentration is given by Saha's equation (Reference 4).

$$n_e^2 = \left(\frac{2 \pi m_e k T_e}{h^2} \right)^{3/2} (n_a - n_e) e^{-\frac{1}{k T_e}} \quad (18)$$

For a mixture of an inert carrier gas seeded with an easily ionizable gas, the electrical conductivity is (Reference 4).

$$\begin{aligned} \frac{1}{\sigma} = & \frac{m_e}{e^2 n_e} \left(\frac{3 k T_e}{m_e} \right)^{1/2} \left[n_n Q_n + (n_a - n_e) Q_a \right] \\ & + \frac{1}{32 \pi} \frac{e^2}{m_e \epsilon_0^2} \left(\frac{m_e}{2 k T_e} \right)^{3/2} \ln \left[\frac{12 \pi}{e^3} \frac{(\epsilon_0 k T_e)^{3/2}}{\sqrt{n_e}} \right] \end{aligned} \quad (19)$$

These equations can be solved by the method of similarity used in Reference (2). However, the results are not general in that the free stream velocity and static pressure must vary in a particular way. More general but less accurate solutions can be obtained by using integral methods, in which the velocity and static temperature distributions through the boundary layer are approximated by polynomials of a degree sufficient to satisfy the appropriate boundary conditions.

The solution, which was essentially an extension of the work of Reference (5) to include the electromagnetic terms, was quite general in that arbitrary pressure and surface temperature gradients and an arbitrary but constant Prandtl number were allowed. Originally, the assumption was made both in Reference (5) and in a similar Marquardt program that the thermal boundary layer thickness Δ was always greater than the dynamic boundary layer thickness δ . Since this is not necessarily true for the system under investigation, a revised IBM 704 program was written to include cases where Δ is less than δ . A test case was run with $\Delta^* < 1$ where Δ^* is defined as the ratio of the thermal boundary layer thickness Δ and the dynamic boundary layer thickness δ . However, the computer stopped itself after the numerical integration had progressed only a short distance down the accelerator

channel. Investigations of the available data showed that the problem occurs where the machine must simultaneously solve four coupled, non-linear algebraic equations for the temperature gradient at the wall, two temperature profile form factors and Δ^* . To show the complexity of these equations and a method to arrive at a solution, the equations will simply be stated here.

$$\dot{g}(\bar{x}, 0) = -2\lambda_{t_0} + \dot{g}_1(0)\lambda_{t_1} - \frac{1}{60}\lambda_{t_2} \quad (20)$$

$$\lambda_{t_1} = \Delta^{*2} \lambda_{t_1}^* = \Delta^{*2} \left\{ Pr \frac{u_\infty^2}{c_p T_\infty} \left[\dot{f}(\bar{x}, 0) \right]^2 + \frac{Pr (R_0 \delta^2)}{\frac{\rho_\infty}{\rho_0} \left(\frac{\mu}{T} \right)_w} \right. \\ \left. \left[\frac{\pm \frac{5}{2} j k T_\infty}{e \rho_0 u_\infty c_p T_\infty} \frac{\dot{g}(\bar{x}, 0)}{\delta \Delta^* \Gamma} + \frac{j^2 l}{\sigma_w \rho_w u_w c_p T_\infty} \right] \right\} \quad (21)$$

$$\lambda_{t_2} = \Delta^{*3} \lambda_{t_2} = \Delta^{*3} \left\{ \frac{Pr (R_0 \delta^2)}{\frac{\rho_\infty}{\rho_0} \left(\frac{\mu}{T} \right)_w} \left\{ T_w^* \left[\frac{T_w^*}{T_w^*} + \frac{T_\infty'}{T_\infty} + 3 \frac{u_\infty^2}{c_p T_\infty} \frac{u_\infty}{u_\infty} - \frac{j B l}{Pr c_p T_w} \right] \dot{f}(\bar{x}, 0) \right. \right. \\ \left. \left. - \frac{1}{\delta \Delta^{*2} \Gamma} \frac{(\pm \frac{5}{2} j k T_\infty)}{e \rho_0 u_\infty c_p T_\infty} \left[\frac{\Delta^2 \Gamma}{T_\infty} \frac{\partial^2 T_e}{\partial \eta^2} \right]_w - \frac{1}{2 \Delta^* \Gamma T_w^*} \right. \right. \\ \left. \left. \frac{T_w j^2 l}{T_{e_w} \sigma_w \rho_w u_\infty c_p T_\infty} \dot{g}(\bar{x}, 0) \left[2 - \frac{T_w}{T_{e_w}} \left(\frac{3}{2} + \frac{I}{k T_\infty T_w^*} \frac{T_w}{T_{e_w}} \right) \right] \right\} \right\} \quad (22)$$

$$\Theta^* = \frac{T_\infty}{T_{t_\infty}} \left\{ \lambda_{t_0} H_0(\Delta^*) + \lambda_{t_1}^* H_1(\Delta^*) + \lambda_{t_2}^* H_2(\Delta^*) \right. \\ \left. + \lambda_1 \left[\lambda_{t_0} H_3(\Delta^*) + \lambda_{t_1}^* H_4(\Delta^*) + \lambda_{t_2}^* H_5(\Delta^*) \right] \right\} \\ + \frac{u_\infty^2}{2 c_p T_{t_\infty}} \left[-0.1845 + 0.00109 \lambda_1 + 0.000114 \lambda_1^2 + 0.00000161 \lambda_1^3 \right] \quad (23)$$

For a given Δ^* , equations 20, 21 and 22 are solved for λt_2 and then λt_1 is obtained from equation 21. Knowing λt_1 and λt_2 , equation 20 can then be solved for $\dot{g}(\vec{x}, 0)$. λt_1 , λt_2 and $\dot{g}(\vec{x}, 0)$ are then inserted into equation 23 to check whether the left hand side (known from another equation) equals the right hand side. If equation 23 is not satisfied then a new value for Δ^* is used and the entire process is repeated until a solution for equation 23 found.

Numerous calculations were performed with the IBM 704 computer but no correct solutions could be obtained. To arrive at a solution to equations 20-23 it would be necessary to find the error in the present program. This involves a slow and arduous hand calculation which was not carried out because the analytical portion was deleted from the program.

B. Kinetic Theory Analysis

The kinetic theory analysis performed during 1962 resulted in a simple relationship for the differential thrust acquired as a consequence of any given increment of power.

$$\frac{d(\text{thrust})}{d(\text{Power})} = \frac{(\text{discharge volume}) (\mu_i + \mu_e)}{\phi \sigma_f} \quad (1)$$

μ_i and μ_e are the ion and electron friction terms respectively, ϕ is the ionization potential and σ_f is the flow cross section of the discharge. This approximation considered only the power required to ionize additional atoms needed for a given increment of thrust.

The minimum tolerable voltage gradient E_A , if "blow out" is to be avoided, is given by the following expression:

$$E_A = \frac{VH}{c} + \frac{\sigma_f \phi H}{a L \mu_{ie}} + 2 \sqrt{\frac{\sigma_f}{a L} \left[\left(\frac{e}{c} H \right)^2 + \mu_i \mu_e \right]} \frac{V}{e^2 \mu_i} \quad (2)$$

where V is the stream velocity, H is the magnetic field strength, c is the velocity of light and a is the discharge cross section.

Since the ionization potential, ϕ , appears in Equations

(1) and (2), both the thrust to power ratio and the blow out condition can be improved. A comparison of ionization potentials of noble gases with those of alkali earths clearly shows (see table below) that the thrust to power ratio can be improved by a factor of 4. Furthermore, the presence of ϕ in the second term of Equation (2) causes a decrease in the externally applied field gradient E_A .

	<u>IONIZATION</u>	<u>MASS</u>
He	24.6	4.0
Li	5.3	6.9
Ne	21.6	20.2
Na	5.1	23.0
A	15.8	40.0
K	4.3	39.1
Kr	14.0	83.8
Rb	4.2	85.5
Xe	12.1	131.3
Cs	3.9	132.9

At low ionization potentials, thermal ionization may be important enough to completely change the character of the analysis. Saha's equation (3), for thermal ionization assumes that ions, electrons and neutrals are in thermal equilibrium. Conditions in either an arc jet or a $\vec{J} \times \vec{B}$ accelerator are far from equilibrium, which permits operation of a $\vec{J} \times \vec{B}$ device at relatively low gas temperatures. Equation (3) gives a lower bound on ionization and indicates the amount of energy stored in the heat of the gas that is available for producing ionization. Saha's equation is given by:

$$\frac{X^2}{1-X^2} = 3.16 \times 10^{-7} T^{2.5} e^{-\frac{e\phi}{kT}} = f \quad (3)$$

where $X = \frac{n_i}{n}$ is the fraction of atoms ionized, p = total pressure-atm, T = temperature - °K, $e = 1.6 \times 10^{-19}$ coulomb, ϕ = ionization potential-ev, k = Boltzman's constant - 1.38×10^{-23} joules/°K.

For X near 1 (complete ionization) an approximate expression for x is:

$$X \approx 1 - \frac{P}{2f} \quad (4)$$

and for X near 0 (no ionization):

$$X \approx \left(\frac{f}{P}\right)^{\frac{1}{2}} \quad (5)$$

The results are quite temperature sensitive. Assuming a pressure of 10^{-2} atmospheres and a temperature of 3000°K , Equation (5) gives only 6% ionization while at the same pressure and 5000°K , Equation (4) yields 87% ionization. These results suggest that in a seeded accelerator, ionization could extract energy primarily from the heat content of the gas and only secondarily from ionizing collisions with electrons. If ϕ is 4 ev/ion then for 1% seeding 10^{-2} ev/atom will be produced. Therefore, 4 ev/ion $\times 10^{-2}$ ions/atom = 4×10^{-2} ev/atom will be expended in ionization. Since the gas has approximately 0.3 ev/atom of thermal energy, the ionization energy is only a small fraction of the energy available. If the ionization takes place in the arc jet, no particular advantage accrues to thermal ionization since this energy must be replaced by the arc jet if the entrance velocity into the $\vec{J} \times \vec{B}$ section is to be as high as possible. On the other hand, if the ionization occurs after the gas has left the arc jet the energy will come from random thermal energy, most of which could not be recovered.

Another consideration of possible importance is the effect of the ion/atom mass ratio on the friction terms, μ_i and μ_e , in Equations (1) and (2). A large difference in masses leads to poor momentum and energy exchange. The implications of this mismatch have not been thoroughly explored as yet but, in general, it would appear advisable to use a seeding element of nearly the same mass as that of the gas.

All modes of energy transfer will be affected by the addition of a seeding element. Effects which must be considered to some approximation include the cathode and anode sheaths and cathode and anode work functions, radiation losses, energy frozen in excited atomic or molecular states, convective heat transfer, and defocusing mechanisms such as the Hall effect.

C. Hall Effects and Methods of Reducing Them

One of the major problems in a $\vec{J} \times \vec{B}$ magnetogasdynamic accelerator is beam deflection which is caused by interaction of Hall currents with the magnetic field. In order to maximize the thrust of such an accelerator, beam deflection must be eliminated or at least minimized, i.e., the axial current or Hall currents have been proposed. The most promising method to date which was reported by Blackman (6) and Lenn, et al (7) is to provide an axial potential opposing the Hall potential by proper staggering of accelerator electrodes.

D. Symbols

B	Magnetic flux density
c_p	Specific heat at constant pressure
α	Constant in eq. 17
e	Charge on electron
h	Planck's constant
H_a	Hartmann number $\equiv \left[\frac{\sigma B^2 \ell^2}{\mu} \right]^{\frac{1}{2}}$
I	Ionization potential of seed gas
j	Current density
k	Boltzmann's constant
K	Thermal conductivity
ℓ	Characteristic length
m	Mass
M	Mach number
n	Particle density
p	Static pressure
P_r	Prandtl number
Q	Collision cross-section
R_e	Reynolds number
R_n	Magnetic Reynolds number

T	Temperature
u	Velocity parallel to surface
v	Velocity perpendicular to surface
x	Dimension parallel to surface
y	Dimension perpendicular to surface
γ	Ratio of specific heats
δ	Boundary layer thickness
ϵ_0	Permittivity of free space
μ	Viscosity
μ_0	Permeability of free space
ρ	Density
σ	Electrical conductivity
$f(\bar{x}, \bar{\eta})$	Velocity profile
$g(\bar{x}, \bar{\eta})$	Temperature profile
Δ^*	$\frac{\Delta}{\delta}$
Δ	Thermal boundary layer thickness
δ	Dynamic boundary layer thickness
$\lambda_{t_1}, \lambda_{t_2}$	Temperature profile form factors
Θ	Thickness parameter
$H_1(\Delta^*)$	Universal function of Δ^*
Γ	$\frac{T_w}{T_{e_w}} \left[1 + \left(1 - \frac{T_w}{T_{e_w}} \right) \left(\frac{3}{2} + \frac{I T_w}{k T_\infty T_w^* T_{e_w}} \right) \right]$

Sub - and Superscripts

e	Electron
w	Conditions at body surface
t	Stagnation conditions
∞	Free stream conditions
o	Local free stream conditions
$\left\{ \begin{matrix} \vec{} \\ \end{matrix} \right\}^*$	Dimensionless
(\cdot)	Differentiation with respect to $\bar{\eta}$ or $\bar{\eta}_1$
($$)'	Differentiation with respect to x or \bar{x}

E. REFERENCES

1. Gates, G. C., et al, "Loss Mechanisms of a Low Temperature Plasma Accelerator", ARS, Vol. 32, No. 4, April 1962.
2. Kerrebrock, J. L., "Electrode Boundary Layers in Direct-Current Plasma Accelerators", J. Aerospace Science, Vol. 28, No. 8, August 1961.
3. Jack, J. L. and Phelps, A. V., "Drift Velocities of Slow Electrons in Helium, Neon, Argon, Hydrogen, and Nitrogen", Physical Review, Vol. 121, No. 3, February 1, 1961.
4. Kerrebrock, J. L., "Conduction in Gases with Elevated Electron Temperature", Engineering Aspects of Magnetohydrodynamics, Munn, N. and Mather, C. W., eds., Columbia University Press, New York 1962.
5. Morris, D. N. and Smith, J. W., "The Compressible Laminar Boundary Layer with Arbitrary Pressure and Surface Temperature Gradients", J. Aerospace Science, Vol. 20, No. 12, December 1953.
6. Blackman, V. H., "Crossed Field Accelerators", ARS Paper 2128-61.
7. Lenn, P., et al, "Three-Fluid Nonequilibrium Plasma Accelerators", Part II, AIAA Paper 63047, 1963.

DISTRIBUTION LIST FOR SUMMARY REPORT

CONTRACT NAS3-2514

Address

1. National Aeronautics and Space Administration (2)
FOB - 10B
600 Independence Avenue, N.E.
Washington, D. C.
Attn: RNT/J. Lazar
2. NASA, Lewis Research Center (2)
21000 Brookpark Road
Cleveland, Ohio 44135
Attn: J. H. Childs
Spacecraft Technology Division
3. NASA, Lewis Research Center (1)
21000 Brookpark Road
Cleveland, Ohio 44135
Attn: Electric Propulsion Lab./G. Seikel
4. NASA, Lewis Research Center (1)
21000 Brookpark Road
Cleveland, Ohio 44135
Attn: Electric Propulsion Lab./W. Moeckel
5. NASA, Lewis Research Center (1)
21000 Brookpark Road
Cleveland, Ohio 44135
Attn: Electric Propulsion Lab./E. Reshotko
6. NASA, Lewis Research Center (1)
21000 Brookpark Road
Cleveland, Ohio 44135
Attn: Technology Utilization Office
7. NASA, Lewis Research Center (1)
21000 Brookpark Road
Cleveland, Ohio 44135
Attn: Spacecraft Technology Procurement Section/John H. DeFord
8. NASA, Lewis Research Center (1)
21000 Brookpark Road
Cleveland, Ohio 44135
Attn: Spacecraft Technology Division/N. J. Stevens

DISTRIBUTION LIST FOR SUMMARY REPORT (Cont'd.)

Address

9. NASA, Lewis Research Center
21000 Brookpark Road
Cleveland, Ohio 44135
Attn: Technical Information Division (1)
10. Commander
Aeronautical Systems Division
Wright-Patterson AFB, Ohio
Attn: AFAPL (APIE)/Lt. Robert Supp (1)
11. NASA, Lewis Research Center
21000 Brookpark Road
Cleveland, Ohio 44135
Attn: Library (2)
12. NASA, Langley Research Center
Langley Air Force Base, Virginia
Attn: M. Ellis (1)
13. NASA, Marshall Space Flight Center
Huntsville, Alabama
Attn: E. Stuhlinger (M-RP-DIR) (1)
14. NASA, Ames Research Center
Moffet Field, California 94035
Attn: G. Goodwin (1)
15. Jet Propulsion Laboratory
Institute of Technology
Pasadena, California
Attn: J. J. Paulson (1)
16. Office of Scientific Research, USAF
Washington 25, D. C.
Attn: Dr. M. Slawsky (SRHP) (1)
17. General Electric Company
Space Sciences Laboratory
Missile and Space Vehicle Dept.
Valley Forge, Pennsylvania
Attn: Dr. P. Gloersen (1)
18. Magnetohydrodynamics, Inc.
P. O. Box 1815
Newport Beach, California
Attn: Dr. V. Blackman (1)

DISTRIBUTION LIST FOR SUMMARY REPORT (Cont'd.)

Address

19. General Dynamics/Astronautics
P. O. Box 1128
San Diego, California 92112
Attn: C. A. Lynch
Mail Zone 110-00 (1)
20. Aerospace Corporation
P. O. Box 95085
Los Angeles, California 90045 (1)
Attn: Library Technical Documents Group
21. Aeronutronics - Ford Motor Company
Newport Beach, California
Attn: D. S. R. Byron (1)
22. Plasmadyne Corporation
3839 South Main Street
Santa Ana, California
Attn: Dr. A. C. Ducati (1)
23. Northrop Corporation
Hawthorne, California
Attn: Dr. P. D. Lenn (1)
24. Allison Division, GMC
Indianapolis, Indiana
Attn: T. L. Rosebrock (1)
25. Radio Corporation of America
Astro-Electronics Division
Princeton, New Jersey
Attn: T. T. Reboul (1)
26. Republic Aviation Corporation
Plasma Propulsion Laboratory
Framingdale, Long Island, New York
Attn: A. E. Kunen (1)
27. TRW Space Technology Laboratories
Thompson Ramo Wooldridge Inc.
One Space Park
Redondo Beach, California
Attn: Dr. C. L. Dailey (1)

DISTRIBUTION LIST FOR SUMMARY REPORT (Cont'd.)

Address

28. United Aircraft Corporation
Research Laboratories
East Hartford 8, Connecticut
Attn: R. G. Meyerand (1)
29. TAPCO Division of Thompson Ramo
Wooldridge Inc.
7209 Platt Avenue
Cleveland 4, Ohio
Attn: R. T. Craig (1)
30. Rocketdyne
6633 Canoga Avenue
Canoga Park, California
Attn: Dr. H. Noeske (1)
31. Rocket Research Corporation
233 S. Holden Street
Seattle 8, Washington
Attn: M. E. Maes (1)
32. Lockheed Missile Systems Division
Palo Alto, California
Attn: D. Bershader (1)
33. Graduate School of Aeronautical Engineering
Cornell University
Ithaca, New York
Attn: Professor E. L. Resler, Jr. (1)
34. Case Institute of Technology
10900 Euclid Avenue
Cleveland, Ohio 44106
Attn: Professor O. K. Mawardi (1)
35. Massachusetts Institute of Technology
Naval Supersonic Laboratory
Cambridge, Massachusetts
Attn: T. K. Kerrebrock and E. E. Covert (1)
36. Rensselaer Polytechnic Institute
Troy, New York
Attn: Dr. E. H. Holt (1)

DISTRIBUTION LIST FOR SUMMARY REPORT (Cont'd.)

Address

- 37. General Electric Company
Flight Propulsion Laboratory
Evandale, Ohio
Attn: Dr. M. L. Bromberg (1)
- 38. General Technology Corporation
3510 Torrance Boulevard
Torrance, California
Attn: Dr. Lee Helflinger (1)
- 39. Electro-Optical Systems, Inc.
125 North Vinedo Avenue
Pasadena, California (1)
Attn: Dr. T. M. Teem
- 40. AFWL
Kirtland Air Force Base, New Mexico
Attn: WLPC/Capt. C. F. Ellis (1)
- 41. Westinghouse Astronuclear Laboratories
Pittsburgh 34, Pennsylvania
Attn: Mr. H. W. Szymanowske, Manager
Electrical Propulsion Laboratory (1)
- 42. AVCO Corporation
Research and Advanced Development Division
Wilmington, Massachusetts
Attn: Dr. Richard John (1)
- 43. Space Sciences, Inc.
301 Bear Hill Road
Waltham, Massachusetts 02154
Attn: Joseph M. Proud (1)
- 44. NASA - Scientific and Technical Information Facility
Box 5700
Bethesda, Maryland 20014
Attn: RWP-2448/NASA Representative (6)*

* Plus a reproducible

INTERNAL DISTRIBUTION LIST FOR SUMMARY REPORT

CONTRACT NAS3-2514

1. A. R. Asam (1)
2. J. W. Braithwaite (1)
3. K. B. Cheney (1)
4. W. R. Cunningham (1)
5. R. E. Fisher (1)
6. G. W. Koffer (1)
7. A. J. Kreiner (1)
8. R. E. Marquardt (1)
9. P. J. Papanek (1)
10. R. J. Page (2)
11. A. N. Thomas (1)
12. H. R. Wedell (1)
13. H. W. Welsh (1)
14. File (10)*

* Plus a reproducible